CEBAF Program Advisory Committee Seven Update Cover Sheet

This proposal update must be received by close of business on November 23, 1993 at:

CEBAF
User Liaison Office
12000 Jefferson Avenue
Newport News, VA 23606

FAX: (804) 249-5800

Present Conditionally Approved Proposal Title and Number

Nucleon Structure study by Virtual Compton Scattering

PR- 93-050

Contact Person

Name: Pierre-Y. Bertin
Institution: U. Blaise-Pascal
Address:
Address: (CEBAF)
City, State ZIP/Country:
Phone: (804) 249-7617 **FAX:** (804) 249-7559
E-Mail → Internet: Bertin @ frcpn11

Experimental Hall: A
Total Days Requested for Approval: 22
Minimum and Maximum Beam Energies (GeV): 1.3GeV - 4GeV
Minimum and Maximum Beam Currents (μAmps): 40μA

CEBAF Use Only

Receipt Date: 11/23/93 PR 93-106

By: SO

Nucleon structure study by Virtual Compton Scattering

G. Audit, M. Berheim, G. Fournier, T. Gousset,
P.A.M. Guichon, M. Guidal, N. D'Hose, F. Kunne,
L.Lakehal-Ayat, S. Kerhouas, C. Marchand, J. Marroncle,
J. Martino, J. Mougey, B. Saghai, P. Vernin
DAPNIA/SPhN CE Saclay, France

J. Berthot, P.Y. Bertin, C. Comptour
V. Breton, H. Fonvieille, G. Quemener, O. Ravel
LPC: Univ. Blaise Pascal/IN2P3 Aubiere, France

J. Van de Wiele
IPN Orsay, France

D. Ryckbosh, R. Van de Vyver.
Nucl. Phys.Lab., B9000 Gent, Belgium

C.E. Hyde-Wright, L.B. Weinstein, P. Ulmer.
Old Dominion University, Norfolk VA, 23529, USA

Z.E. Meziani, D. Kawwall
Stanford Univ., Stanford, CA 94305, USA

L. Elouadrhiri
Univ. of Massachusetts, Amherst, MA, 01003 USA

J.M. Finn
College of William and Mary 23187 VA USA

J. Gomez, J. Lerose, R. Michael, S. Nanda, A. Saha
CEBAF, Newport News, VA USA.

and the Hall A collaboration

Abstract

We propose to study nucleon structure by Virtual Compton Scattering using the reaction $p(e,e'p)\gamma$. We will use the Hall A HRS spectrometers to measure the scattered electron and the recoil proton. Compton events will be separated from other channels (principally π^0 production) by the unprecedented missing-mass resolution of the spectrometers. We plan to measure this reaction throughout the resonance region and in the low center of mass energy region.

Spokepersons: P.Y. Bertin, G. Fournier, C.E. Hyde-Wright.

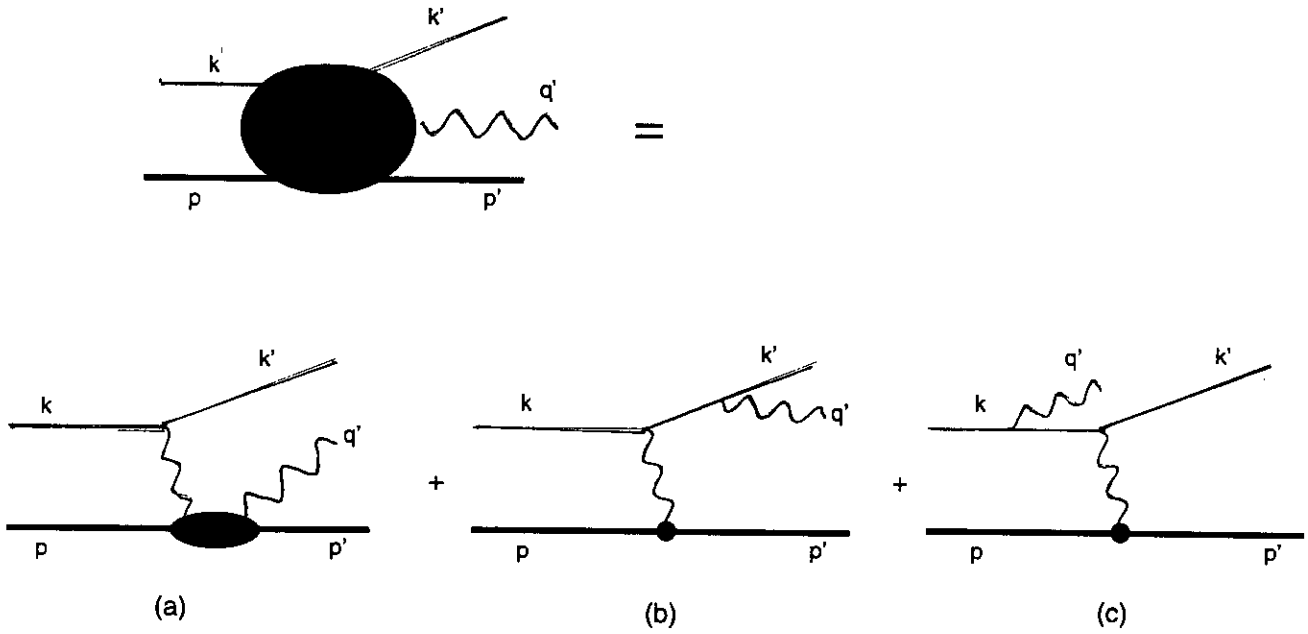

Figure 1: The $p(e,e'p)\gamma$ reaction. The electron and proton momenta are k, k', and p, p', respectively. The final photon momentum is q'. a) The Virtual Compton Scattering (VCS) amplitude. The virtual photon momentum is $q = k - k'$. We use the conventions $p^2 = p'^2 = M^2$, $Q^2 = -q^2$, $s = (p+q)^2$, $t = (q-q')^2 < 0$, and $x_B = Q^2/(2p\cdot q) = Q^2/(s - M^2 + Q^2)$. The angle between q and q' is $\theta^{\gamma^*\gamma}$. b) & c) The Bethe-Heitler (BH) amplitudes. The virtual photon momentum is $q - q' = k - k' - q'$.

1 Introduction

One of the basic problems which remains unsolved is the structure of nucleons in term of quarks and gluons. Despite many efforts, the non perturbative structure of QCD has not yet been understood and it is clear that new experimental data are needed to guide the theoretical approaches, to exclude some scenarios or to constrain the models.

To be useful, the output of the experiment must be amenable to a simple interpretation in terms of elementary degrees of freedom. This is why purely electromagnetic processes are privileged tools since they can be interpreted directly in terms of the current carried by the quarks. In this respect, Virtual Compton Scattering (VCS, see Fig. 1a) which can be accessed through the reaction:

$$e + p \rightarrow e' + p + \gamma \tag{1}$$

is a potentially powerful tool to access nucleon structure. It is the natural complement to form factors, real Compton scattering and deep inelastic scattering.

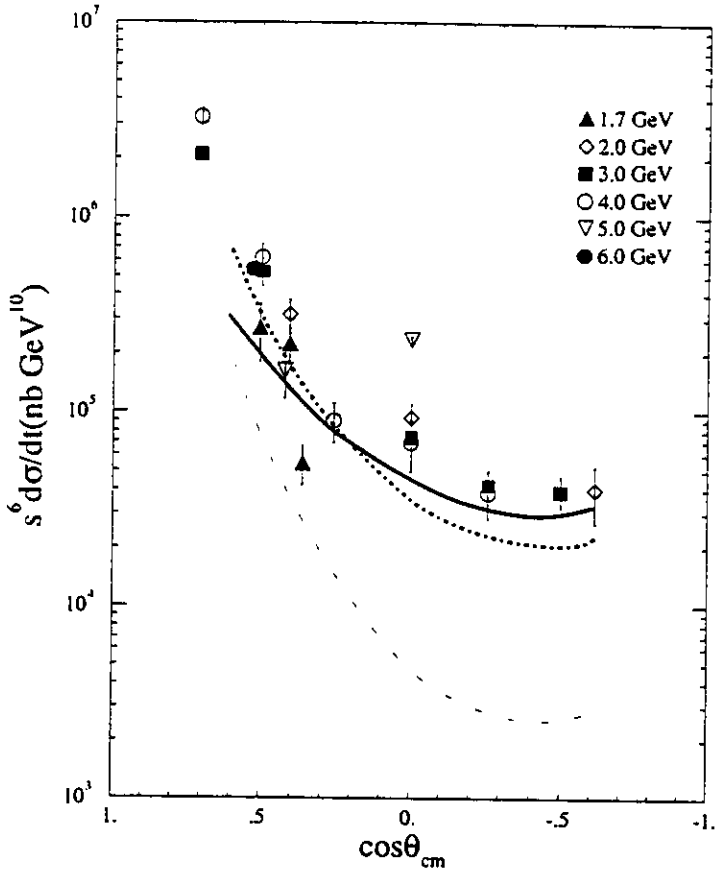

Figure 2: Real Compton scattering. The data are from Refs [1–7]. The curves are from Ref. [10,11,21]

No data exist up to now for this process. Only real Compton scattering has been investigated so far, at Bonn [1] and Tokyo [2, 3] in the resonance region, and Cornell [4, 5], SLAC [6, 7] in the the deep inelastic region and Illinois [32], Saskatoon [29], Mainz [30] in the low energy limit. The low energy data, together with dispersion relations have determined the static electric and magnetic polarizability of the proton. In the resonance region, differential cross sections have been measured at photon center of mass (CM) angles between 40^0 and 160^0 at momentum transfers $t < 1\ GeV^2$ and transverse momenta $p_T < 0.5\ GeV/c$. They indicate a strong forward peaking of the Compton cross section. The data at higher energies are summarized in Figure 2 and show an approximate scaling : ($s^6 d\sigma/dt$ independent of s) consistent with quark counting rules [9]. The t dependence is exponential at small t, but flattens out at CM angles above 90^0.

We propose to investigate the virgin field of VCS at CEBAF by detecting the scattered electron and the recoil proton in coincidence in the HRS spectrometers of hall A. From the

measured momenta k' and p' of the scattered electron and recoil proton, and the incident beam energy E_i, we reconstruct the missing mass M_X. The VCS events are characterized by the photon mass: $M_X = 0$. It is worth mentioning that this program will also serve as a demonstration of the unique CEBAF capabilities. This is illustrated by the comparison of Figure 3a and Figure 3b. On Figure 3 the existing data [12] for the reaction $p(e, e'p)X$ are plotted versus the invariant missing mass. Clearly the photon cannot be distinguished from the π^0. The simulation of our proposed experiment shown in Figure 3b (see section 3.C) clearly indicates that, thanks to the excellent energy resolution, this separation will be possible at CEBAF, thereby allowing VCS experiments without photon detection.

Due to the CM to lab Lorentz boost (see Figure 4) the protons tend to be focused in a small cone around the virtual photon. Thus a large phase space for the real photon is accessible with a single proton spectrometer setting, despite the small solid angle. This helps to keep the counting rate at a reasonable level.

We aim to study VCS in two different kinematical regimes. This is illustrated in Figure 5 First we will study the reaction as a function of s, Q^2, and $\theta^{\gamma^*\gamma}$ in the resonance region. This will provide new insight about both the structure of known resonances and the possible existence of missing resonances. The latter are a long standing problem of the quark model [31]. Second we propose an investigation below the pion threshold. This is a new source of information about nucleon structure because it allows the determination of the quasi-static response functions of the nucleon (as a function of Q^2). These are fundamental observables, analogous to the polarizabilities determined by real Compton scattering. They are on the one hand purely electromagnetic, and on the other hand they do not involve on-shell propagation of the intermediate states. This is an important simplification from the theoretical point of view.

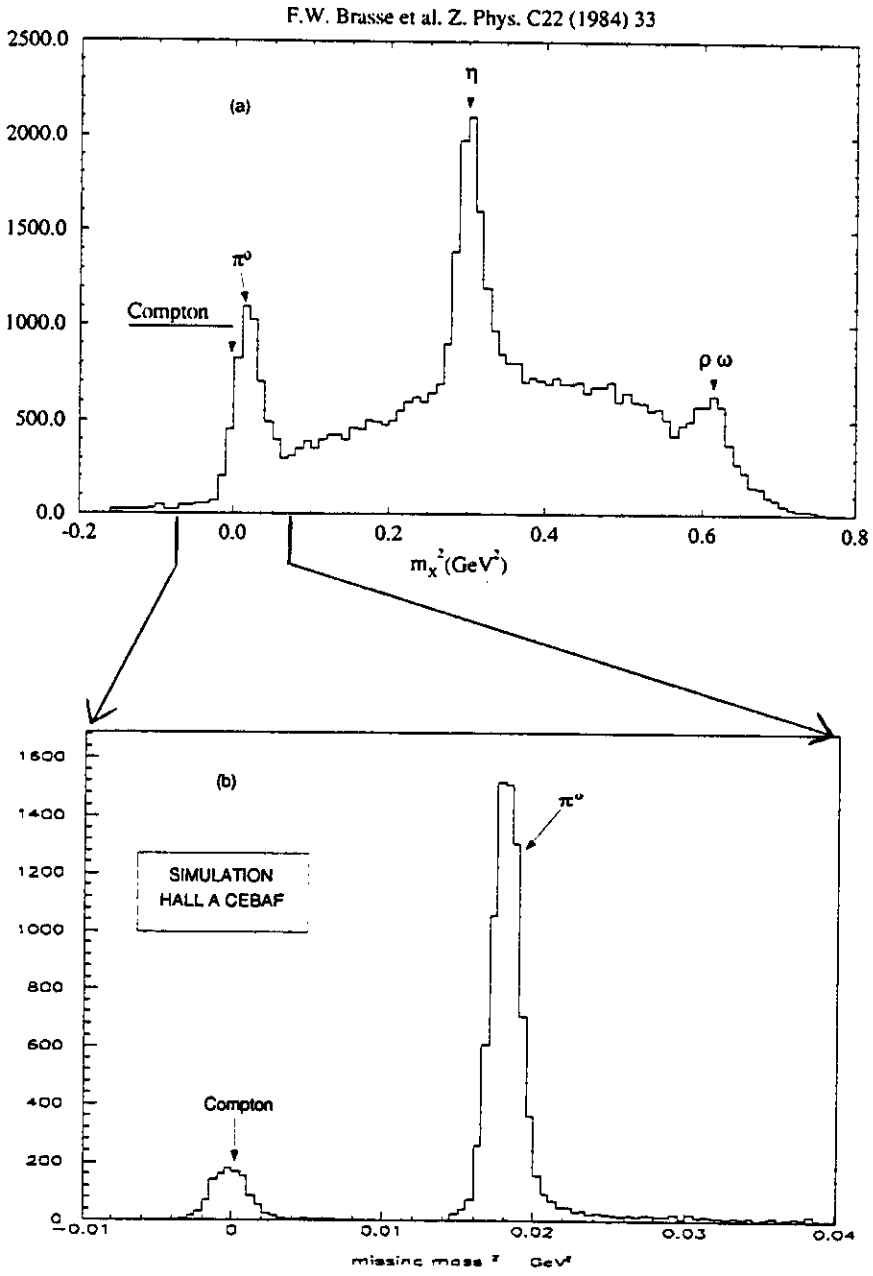

Figure 3: Missing mass squared spectrum for reaction p(e,e'p)X. a) (top) Data of F.W. Brasse et al, Z Phys C22 (1984) 33. b) (bottom) Monte Carlo simulation, Hall A CEBAF. Note that the missing mass scale on b) is greatly expanded from a).

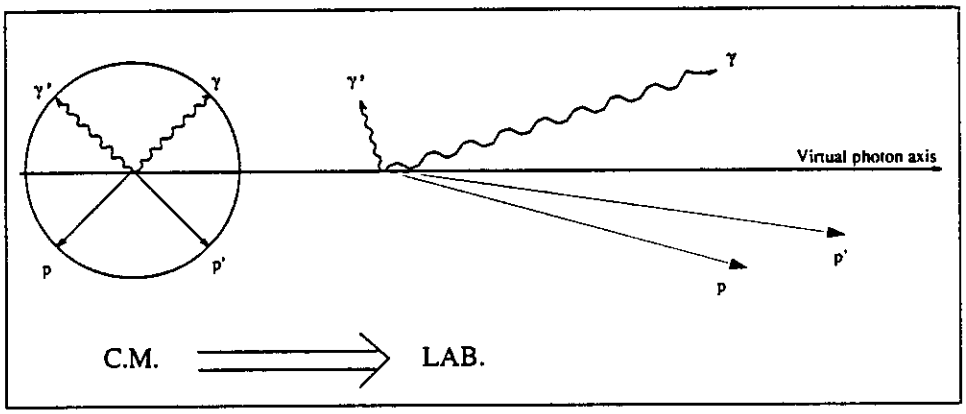

Figure 4: CM to laboratory system Lorentz transformation for final photon and proton for forward scattering ($\gamma\&p$) and backward scattering ($\gamma'\&p'$).

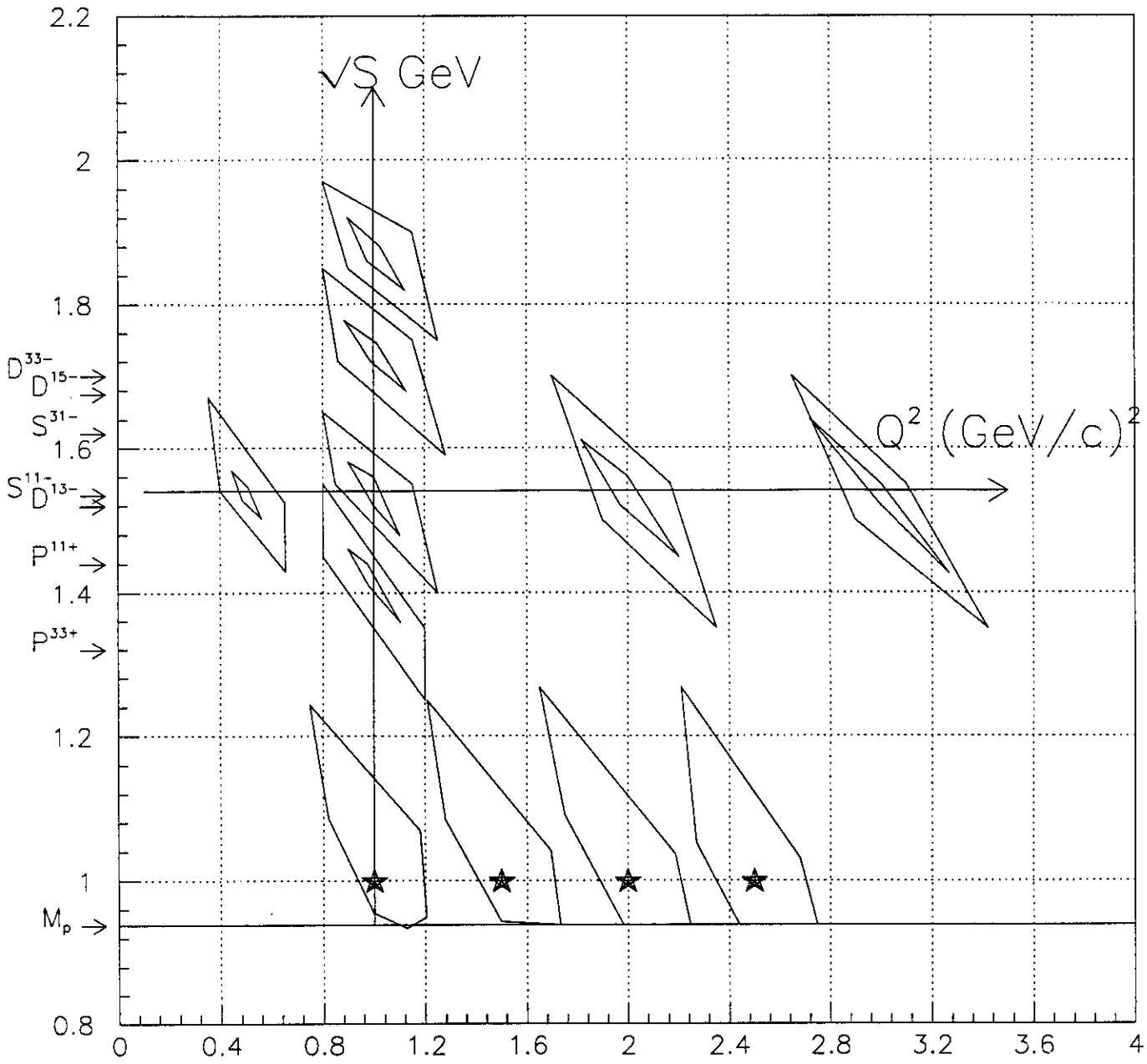

Figure 5: Proposed kinematics for virtual compton scattering measurements. The elongated diamonds indicate the acceptance in s and Q^2 of a single coincidence setup. The double diamonds indicate two settings at different values of ϵ, the longitudinal polarization of the virtual photon in the VCS cross section. At $s = (1.54\ \text{GeV})^2$ and $Q^2 = 1.0$ GeV (indicated by the intersection of the axes) we will measure the in-plane ($\phi = 0°$ and $\phi = 180°$) angular distribution (dependance on $\theta^{\gamma^*\gamma}$). The other measurements for $s > (M + m_\pi)^2$ will be centered at $\theta^{\gamma^*\gamma} = 180°$ The points with stars indicate kinematics below pion threshold. For these points, over 50 percent of the photon phase space is contained in the proton acceptance.

2 Theoretical aspects and program presentation

The experiment will measure the cross section for exclusive electroproduction of a real photon. To lowest order in $\alpha \sim 1/137$ the process is described by the coherent sum of the amplitudes shown in Figure 1. In the following, γ^* or γ^v will denote the virtual photon of the VCS process. We denote by $\theta^{\gamma^*\gamma}$ the angle between γ^* and the real photon. Our convention is that the azimuthal angle of the latter is $\phi = 0^0$ when it is emitted in the same half plane as the scattered electron.

In Fig.1, VCS refers to amplitude a) while b), & c) describe the Bethe-Heitler (BH) process which is exactly calculable from QED provided the elastic form factors $G_M^p(-t)$ and $G_E^p(-t)$ are known. This is the case in the energy range of CEBAF. As is well known the BH process is strongly peaked along the electron lines. This allow us to define regions for the final photon where BH is either dominant, either negligible, or of the same order of magnitude as VCS. This is illustrated on Figure 6. When the BH and VCS amplitudes are of comparable magnitude, the interference term will be important.

Since the BH amplitude is calculable, its interference with VCS is a new source of information. In particular above pion threshold it is sensitive to the phase of the Compton amplitude. However a quantitative study requires out of plane experiments which are possible only in the low energy region. In the resonance region we will make a tentative exploration of interference region but most of the measurements will be performed at $\theta^{\gamma^*\gamma} = 180°$ where the BH is negligible compared to the predicted VCS. It is worth mentioning that in the interference region, the usual transverse-longitudinal decomposition of the cross section is no longer valid since the symmetry around the virtual photon is broken by the second photon coupling to the electron.

In the rest of this section we discuss only the VCS amplitude. To lowest order in α the amplitude is defined by (helicity labels are omitted for simplicity):

$$T_{VCS} = \int d^4x e^{i(q+q')\cdot x/2} \epsilon^{*\mu}(q') \langle p' | T\left[J_\mu(x/2) J_\nu(-x/2)\right] | p \rangle \epsilon^\nu(q) \qquad (2)$$

with $T[\ldots]$ the time-ordering operator, $\epsilon^{*\mu}(q')$ the complex conjugate of the polarization vector of the outgoing photon, $\epsilon^\nu(q) = \bar{u}(k')\gamma^\nu u(k)$ the polarization vector of the incident virtual photon, and J_μ the electromagnetic current of the proton. In terms of quark fields:

$$J_\mu = \sum_{f \in \text{flavors}} e_f \bar{\psi}_f \gamma_\mu \psi_f, \qquad e_u = (2/3)e, \ldots \qquad (3)$$

The amplitude T_{VCS} depends on 3 independent invariants. The usual choices are

$$\begin{array}{c} Q^2, \quad s, \quad t \\ \text{or } Q^2, \quad x_B, \quad t \end{array} \qquad (4)$$

It is often convenient to use θ^γ_{CM}, the CM angle of the photon, instead of t.

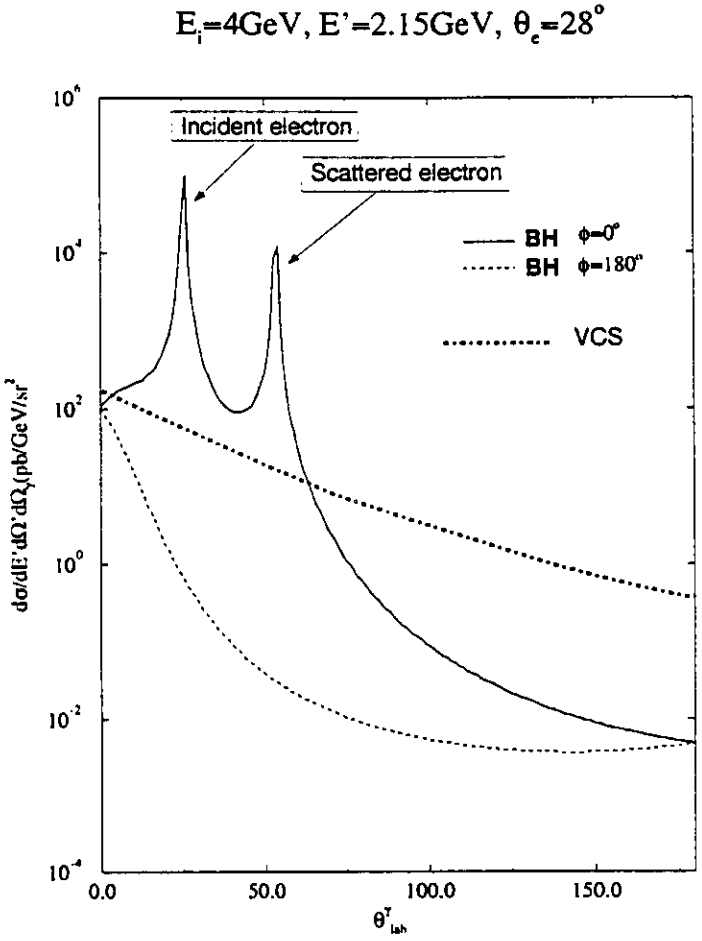

Figure 6: Bethe-Heitler and Virtual Compton scattering cross sections as a function of θ^{γ}_{lab}, as estimated in Section 3. ϕ is the azimuth of the final photon around the VCS virtual photon (q). The VCS cross section is dominant in the backward direction.

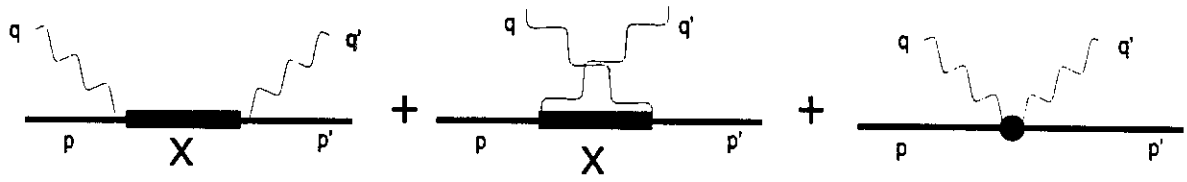

Figure 7: VCS in the resonance region, in the model of Ref. [33,34]. (a) direct term, (b) crossed term and (c) contact term

2.1 Resonance Region

VCS in the resonance region is complementary to both inclusive (e, e') and exclusive $(e, e'$meson electro- (and photo-) production of resonances. Unlike exclusive production, VCS depends only on the electromagnetic couplings $\gamma + N \rightarrow N^*$ and does not depend explicitly on the hadronic couplings $N^* \rightarrow N\pi$, *etc.* Thus any model of resonance structure will be able to make predictions of virtual compton scattering, independent of its ability to describe the resonance decay channels. The inclusive (e, e') cross section is proportional to the imaginary part of the forward compton amplitude (with identical virtual photons in both the initial and final states). Thus the angular distribution of VCS provides a new degree of freedom for the purely electromagnetic study of the resonance region.

Capstick and Keister have calculated real [33] and virtual [34] compton scattering in a harmonic oscillator quark model. In time-ordered perturbation theory, they approximate the VCS amplitude as an explicit sum over simple Breit-Wigner resonances:

In the center of mass Figure 7, the amplitude has the form:

$$\begin{aligned} T^{\mu\nu}_{VCS} &= \sum_X [\text{direct + crossed + contact terms}] \\ &= \sum_X \frac{\langle N(-\vec{q}')|\, J^\mu(0)\, \big|X(\vec{0})\big\rangle \big\langle X(\vec{0})\big|\, J^\nu(0)\, |N(-\vec{q})\rangle}{\sqrt{s} - M_X + i\Gamma_X/2} \\ &\quad + \frac{\langle N(-\vec{q}')|\, J^\nu(0)\, |X(\vec{q}' - \vec{q})\rangle\, \langle X(\vec{q}' - \vec{q})|\, J^\mu(0)\, |N(-\vec{q})\rangle}{q_0 - q_0' + \sqrt{M_N^2 + \vec{q}^2} - \sqrt{M_X^2 + (\vec{q} + \vec{q}')^2} + i\Gamma_X/2} \\ &\quad + \text{contact terms.} \end{aligned} \tag{5}$$

The contact terms are required by gauge invariance. In the resonance region, both the crossed and contact terms are expected to be small, real, and slowly varying with s. The direct term, on the other hand, has contributions from both nearby ($\sqrt{s} \approx M_X$) and distant resonances. It can be seen from Eq. 5 that the contribution of each distant resonances falls

off as $(\sqrt{s} - M_X)^{-2}$ in the imaginary part of the amplitude, but falls only as $(\sqrt{s} - M_X)^{-1}$ in the real part.

Figure 8 shows the real compton data in the backward direction, together with the calculations of [33]. For the $\Delta(1232)$, the quark model transition moment $\mu_{\Delta N}$ is $\approx 30\%$ too small. Since $\mu_{\Delta N}$ enters the real compton cross section in the 4th power, the calculation grossly underestimates the cross section in the Δ region. On the other hand for incident photon energies near 1 GeV, the calculation is in reasonable agreement with the existing data. It should be pointed out that these calculations are without free parameters.

As we seek to understand baryon structure, we are not interested in whether the parameters of a model can be adjusted to fit a particular resonance. Rather, we want to know whether a model can give a reasonable description of the full resonance spectrum, including the electromagnetic couplings. In order to evaluate whether Figure 8 represents a catastrophic failure of the model, or simply a particular difficulty with the Δ-resonance, it is necessary to study VCS over a wide range in Q^2, s, and $\theta_{\gamma\gamma}$. The Q^2 and $\theta_{\gamma\gamma}$ dependence of the model calculations is illustrated in Fig. 9

The calculation in Figure 8 also indicates the sensitivity of VCS to the missing resonances. These are positive parity ($2\hbar\omega$) states predicted by the quark model, but never observed. It is conjectured that these states have very small $N^* \rightarrow N\pi$ couplings [31]. The effect of these resonances on the Compton cross section is large.

The VCS amplitude in the resonance region can also be studied phenomenologically. The nearby resonances in Eq. 5 can be included with explicit experimental couplings extracted from exclusive production measurements. The remaining contribution, from the contact term and from distant resonances, can be parameterized as a smooth background. If the empirical $\gamma_V N \rightarrow N^*$ couplings together with a smooth background term cannot reproduce the VCS cross-section, this may be a signature of missing resonances. The relative magnitudes of this division of the VCS cross section into nearby and distant resonances is a measure of the extent to which resonances are in fact the appropriate degrees of freedom in this mass domain.

For our choice of kinematics in the resonance region, we first fix $\theta^{\gamma^*\gamma} = 180°$ and study VCS as a function of s at fixed Q^2 (Figure 5). We choose $Q^2 = 1.0$ GeV^2, so that Q^2 is large enough that we are sensitive to the short range structure of the resonances, but not so large that the cross sections are unmeasureably small. Similarly, we go to as high s as is practical at an incident energy of 4 GeV. We fix the proton spectrometer at $\theta^{\gamma^*\gamma} = 180°$ to assure that the compton cross section dominates over the BH. Second, we remain at $\theta^{\gamma^*\gamma} = 180°$ and $\sqrt{s} \approx 1.5 GeV$ and study VCS as a function of Q^2. We choose this value of $\sqrt{s}$ in order to be in the region of the S_{11} and D_{13} resonances. These resonances have been studied in inclusive (e, e') and have very different Q^2 dependence. In addition, we choose this region because we wish to study the Q^2 dependence in a region where there are overlapping resonances (in contrast to the Δ-region). Third, we fix $\sqrt{s} \approx 1.5$ GeV and $Q^2 \approx 1.0$ GeV^2 and measure the cross section as a function of $\theta^{\gamma^*\gamma}$ in the electron scattering plane ($\phi = 180°$ and $\phi = 0°$). This permits us to obtain a partial angular distribution of the VCS, and to identify the region of strong interference between the BH and VCS amplitudes.

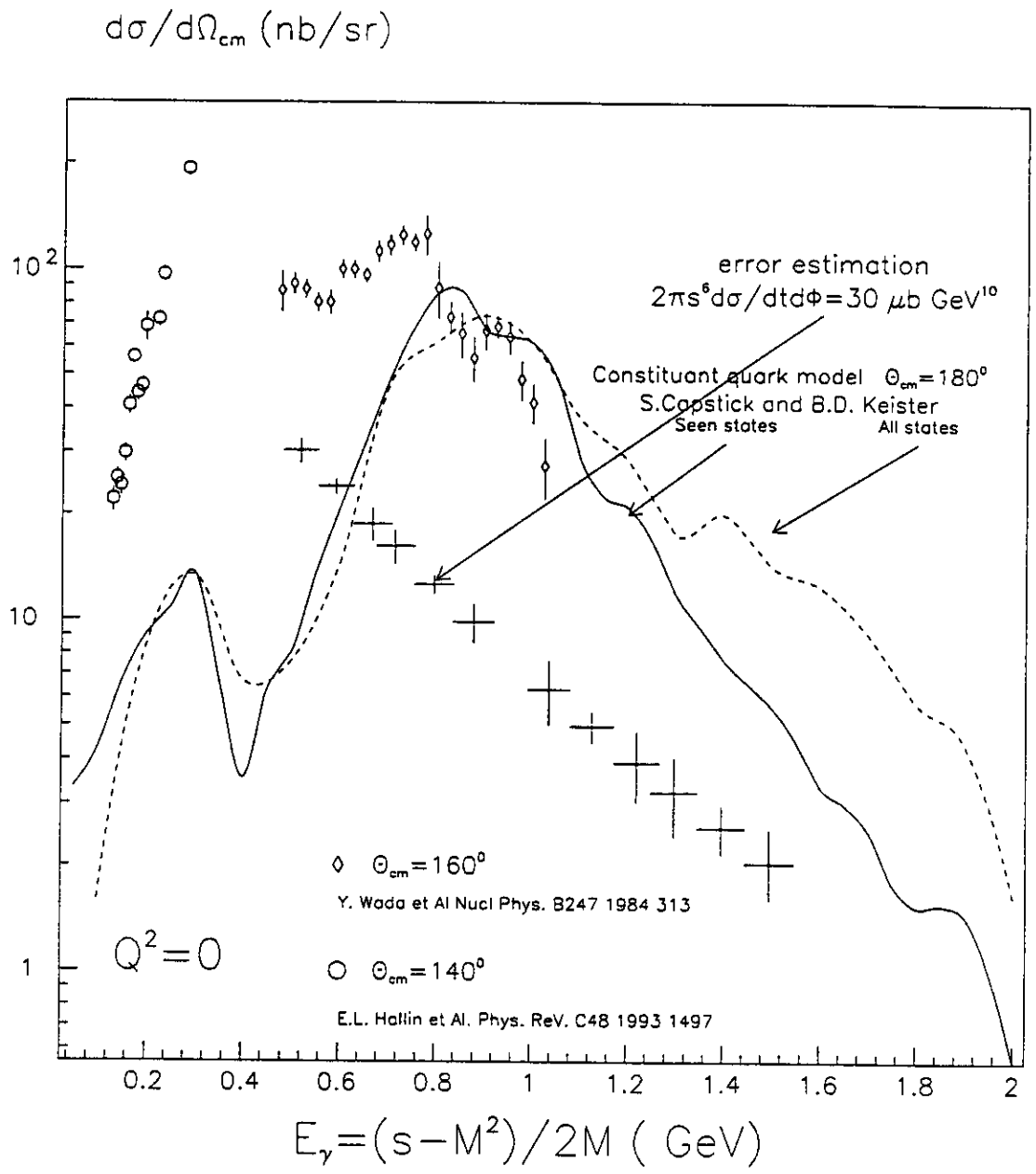

Figure 8: Real Compton Scattering. The open circles and diamonds are real compton scattering measurements in the backward direction. The curves are the non-relativistic quark-model calculations of [33], at $\theta^{\gamma^*\gamma} = 180°$. The solid line is the calculation including the theoretical values only for experimentally observed states. The dashed line is the full calculation, with all $n = 0, 1, 2$ states. The crosses are a cross section and error estimate for VCS at $Q^2 = 1.0GeV^2$. These estimates are discussed in Section 3.

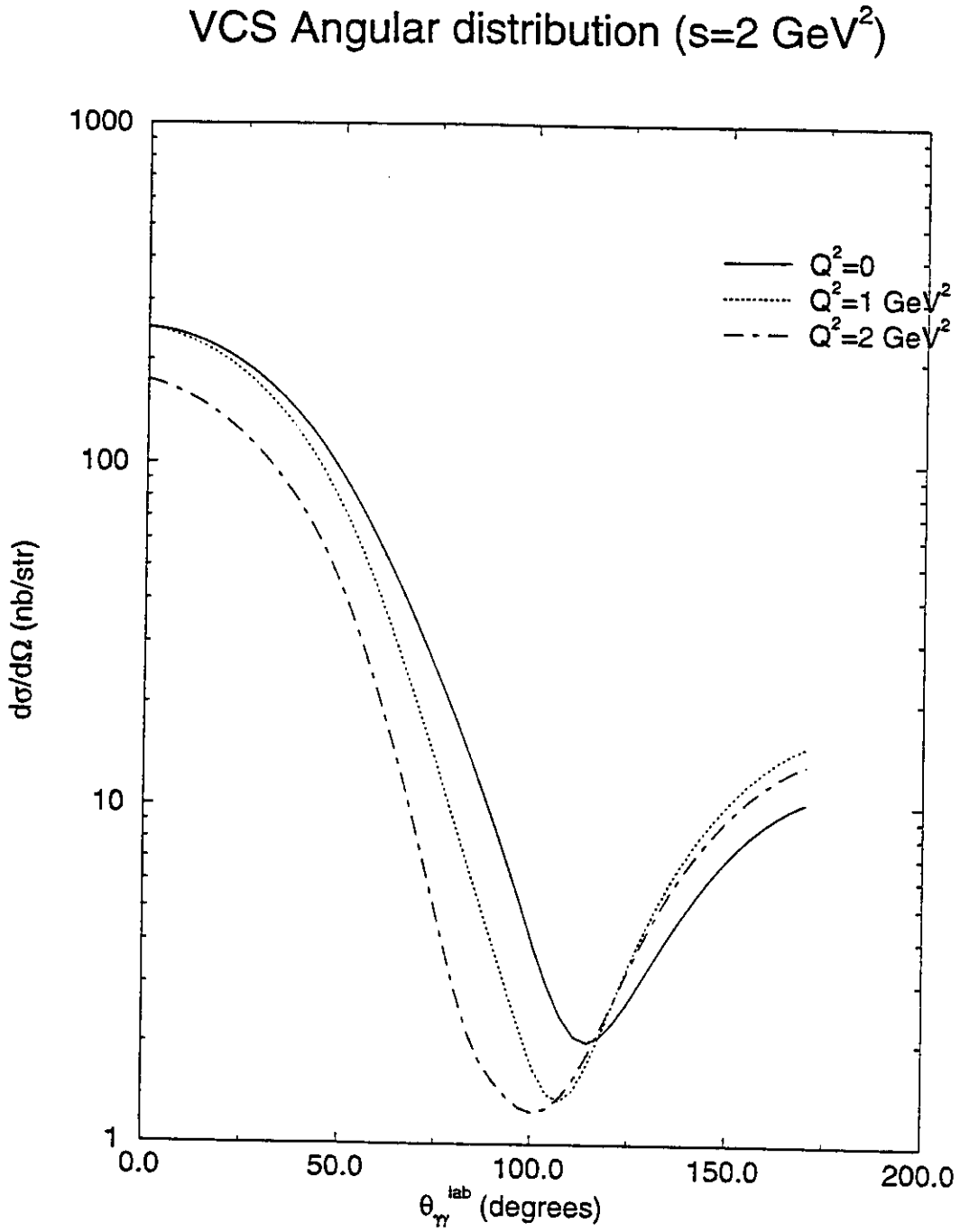

Figure 9: Preliminary results of B.D. Keister and S. Capstick for the Q^2 dependance of the VCS cross section (Ref. [34]).

2.2 Low energy region

The amplitude for a process where a soft photon is emitted with energy q' can be written in terms of the elastic amplitude up to terms linear in q'. This is the content of Low's theorem [28] which gives the terms of order $(q')^{-1}$ and $(q')^0$. This applies to Virtual Compton Scattering and the resulting low energy theorem (LET) is

$$T^{VCS} = \epsilon'^*_\mu T^{\mu\nu}_{\rm LET} \epsilon_\nu + O(q') \tag{6}$$

$$\begin{aligned} T^{\mu\nu}_{\rm LET} &= \bar{u}(p')\Gamma^\mu(-q')\frac{\gamma\cdot(p'+q')+M}{2p'\cdot q'}\Gamma^\nu(q) \\ &+ \bar{u}(p')\Gamma^\nu(q)\frac{\gamma\cdot(p-q')+M}{-2p\cdot q'}\Gamma^\mu(-q')u(p) \end{aligned} \tag{7}$$

$$\Gamma^\mu(K) = F_1(K^2)\gamma^\mu + iF_2(K^2)\frac{\sigma^{\mu\alpha}K_\alpha}{2M} \tag{8}$$

with ϵ' the polarization vector of the final photon and

$$\epsilon^\mu = \bar{u}(k')\gamma^\mu u(k) \tag{9}$$

the virtual photon polarization vector. The correction term $O(q') = \epsilon'^*_\mu O^{\mu\nu}\epsilon_\nu$ is of order q' (and higher powers of q').

This expression is correct, up to terms at least of order q', as long as the one photon exchange approximation is valid. It coincides with the Born term evaluated with the *on mass shell Dirac form factors* F_1 and F_2. This would not be the case if the photon vertices were written with the electric and magnetic form factors.

The deviation from the LET has the following expression.

$$O^{\mu\nu} = \sum_X < N(\vec{p}')|J^\mu(0)|X(\vec{p}'+\vec{q}') > \frac{1}{E(\vec{p}')+q'-E_X(\vec{p}'+\vec{q}')} < X(\vec{p}+\vec{q})|J^\nu(0)|N(\vec{p}) > \tag{10}$$

$$+ < N(\vec{p}')|J^\nu(0)|X(\vec{p}'-\vec{q}) > \frac{1}{E(\vec{p})-q'-E_X(\vec{p}-\vec{q}')} < X(\vec{p}-\vec{q}')|J^\mu(0)|N(\vec{p}) >$$

where the sum over X includes any possible intermediate state except the nucleon itself or the nucleon plus nucleon-antinucleon state. The latter two are indeed already included in $T_{\rm LET}$.

In this section we always consider that the center of mass energy is smaller than the pion threshold. Therefore, in the above expression, the propagators are real as long as the process

can be treated to lowest order of QED, which is already assumed for the validity of the LET. The deviation then vanishes in the $q' \to 0$ limit due to the finite mass gap between the nucleon and and the pion threshold. A simple way to see this is to realize that, as the real photon energy goes to zero, a matrix element of the form $< N|J^0(0)|X >$ is proportional to the matrix element of the total charge and therefore vanishes since X cannot be the nucleon state. The rest follows from current conservation.

After this formal introduction, we now state the interest of an experimental study of the low energy region of VCS.

First, since the LET predicts the absolute cross section in terms of known from factors, we have a firm basis for the counting rates as well as a powerful calibration system of the experiment. In particular we have computed the cross section as a coherent sum of the BH and VCS amplitudes.

Second, studying the deviation from the LET as the CM energy increases will provide invaluable information on the nucleon structure. This is contained in Eq. 10 which is essentially the quasistatic response of the nucleon to the electromagnetic probe. This is the most simple observable after the form factor. It is ideally suited to test nucleon structure models because, below pion threshold, the intermediate states do not propagate on-shell. This is a considerable theoretical simplification since the sum in Eq. 10 can be evaluated safely, even if the model does not describe the coupling of the excited states to the pion-nucleon channel.

In real Compton scattering at low energy, both q an q' are small. The deviation $O^{\mu\nu}$ can then be expanded with respect to both of these momenta and the coefficients of order qq' are the polarizabilities [27] of the nucleon, which are now both determined with a reasonable accuracy.

At finite Q^2 but still small q', a similar expansion can be defined. It is slightly more involved than the real photon case, but still simple enough to allow an interpretation in term of generalized polarizabilities [35]. For instance, if both the initial and final photons are magnetic, then the linear part in q' of $O^{\mu\nu}$ has the transparent form (the time components are deduced from current conservation)

$$O(q') = (\vec{\epsilon}' \times q')^i M_{ij} (\vec{\epsilon} \times q)^j \tag{11}$$

$$M^{ij} \sim \sum_X \left[< N| \int d\vec{r} \mu^i(\vec{r}) |X > \frac{1}{E_N - E_X} < X| \int d\vec{r} \frac{3j_1(qr)}{qr} \mu^j(\vec{r}) |N > \right. \tag{12}$$

$$\left. + < N| \int d\vec{r} \frac{3j_1(qr)}{qr} \mu^j(\vec{r}) |X > \frac{1}{E_N - E_X} < X| \int d\vec{r} \mu^i(\vec{r}) |N > \right]$$

where $\vec{\mu} = \vec{r} \times \vec{J}(\vec{r})$ is the magnetic moment density. When q is small, the Bessel function tends to $qr/3$ and one recognize in M_{ij} the usual expression of the magnetic polarizability. It should be clear that the measurement of these generalized polarizabilities through Virtual

Compton Scattering will enlarge enormously the set of static electromagnetic observables against which the nucleon structure models can be compared.

The study is also important for the longstanding problem of the nucleon structure modification in the nuclear medium. The scale for this effects is basically set by the average off-shellness of bound nucleon, a few tens of MeV. The idea is that the successive interaction of the nucleon with its partners alters its structure. In a quark description that would be depicted as a change in the internal quark wave function with respect to the free situation. A more general statement is that, in the medium, the 'nucleon' becomes a superposition of free nucleon and excited baryonic states. This mixture depends on the interaction and on the way the nucleon responds to the interaction. The second point can be approached by low energy Virtual Compton Scattering because the generalized polarizabilities are the responses to a particular probe. Understanding these responses in a range of energy comparable to the average of off-shellness in nuclei is prerequisite for any model aiming at the description of nuclear matter in term of composite nucleons.

To access the generalized polarizabilities, one needs to measure the linear deviation from the LET. This clearly demands that the latter actually be satisfied. There is little doubt about its validity but we may question the range where it applies, and this *a priori* depends on the kinematics. Therefore we shall study the cross section for several sets of Q^2 and CM scattering angle as a function of decreasing CM energy to determine the range where the LET applies. This calibration of the theory against experiment and vice-versa is a prerequisite step.

It is important to have an initial guess about the range of applicability of the LET. To this aim, we have estimated the corrective term of Eq. 10 using only the delta excitation. We do not expect this to be realistic but it is sufficient as a guide. Figure 10 shows the results for the cross section for several values of the CM energy (BH process is not included here so as to not mix independent effects). We can see that below 0.97 GeV (32 MeV above threshold of VCS) there is hardly any difference between the pure LET case and the (LET + Delta) case. This is why the calibration step will be done at the CM energies ranging from 20 MeV to 50 MeV. An important question about the determination of the generalized polarizabilities is whether the deviation from the LET are large enough below the pion threshold to be measured accurately. The delta excitation models give us a qualitative answer to this question. In figure 10 we can see that its contribution becomes important (50% of the cross section, according to the angle) when the CM energy is 1.05 GeV, that is 30 MeV below pion threshold. To show the sensitivity to magnetic polarizability, we have varied its value by 20% in Fig. 11. To be realistic, we have added coherently the Bethe-Heitler amplitude. We see that a measurement of the cross section at the few % level would clearly distinguish between the two cases. This support the idea that a fruitful study of the low energy VCS region is possible.

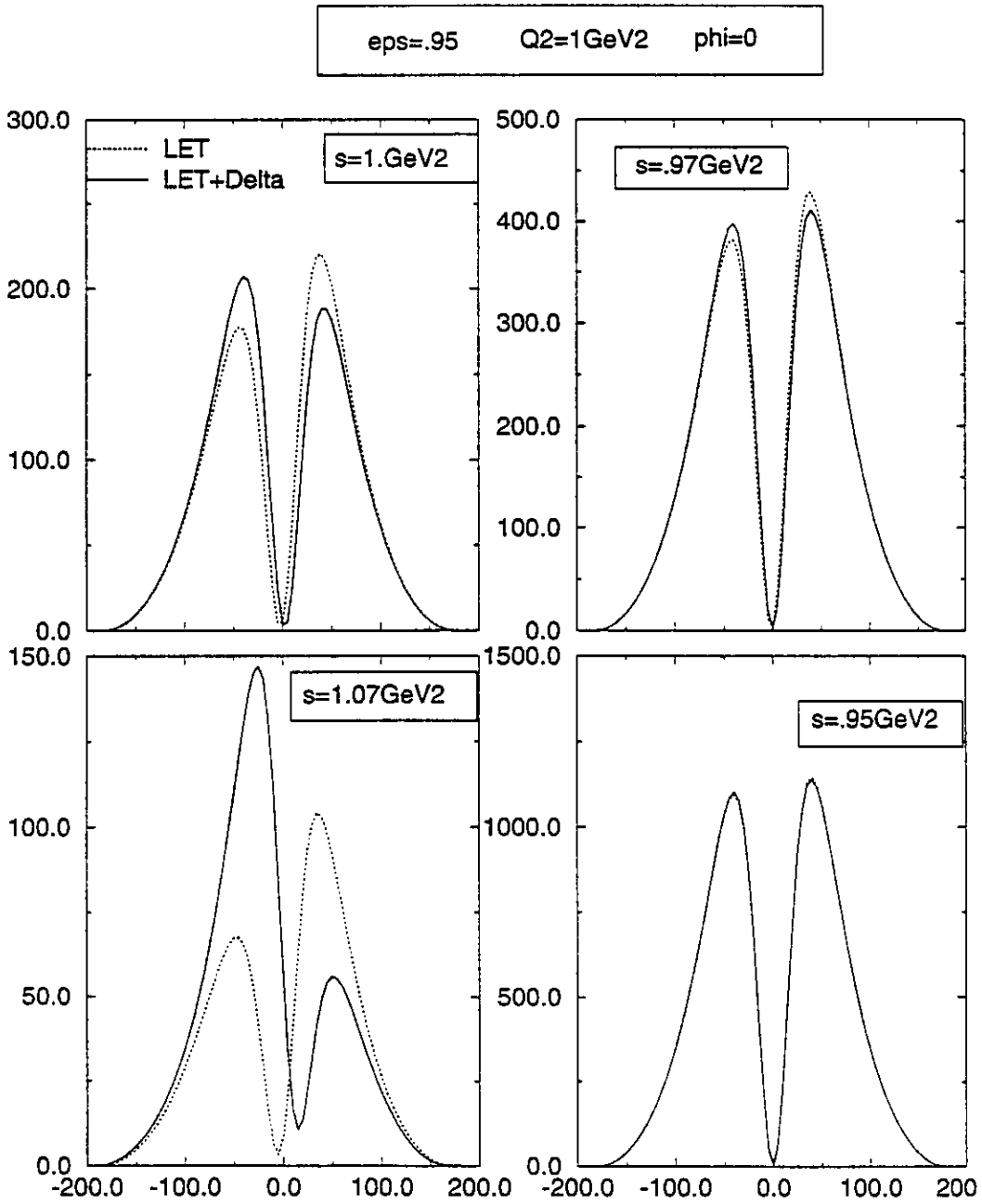

Figure 10: Angular distribution of VCS part of the cross section $d^4\sigma/(dE'_e d\Omega'_e d\Omega'_\gamma)$ (nb GeV^{-1} sr^{-2}) as a function of $\theta^{\gamma^*\gamma}$ for several values of s between $M^2 = 0.88$ GeV^2 and $(M + m_\pi)^2 = 1.15$ GeV^2. The dotted curves are the exact cross section including only the LET (Eq. 7). The solid curves include the correction term (Eq. 10) of just the Δ.

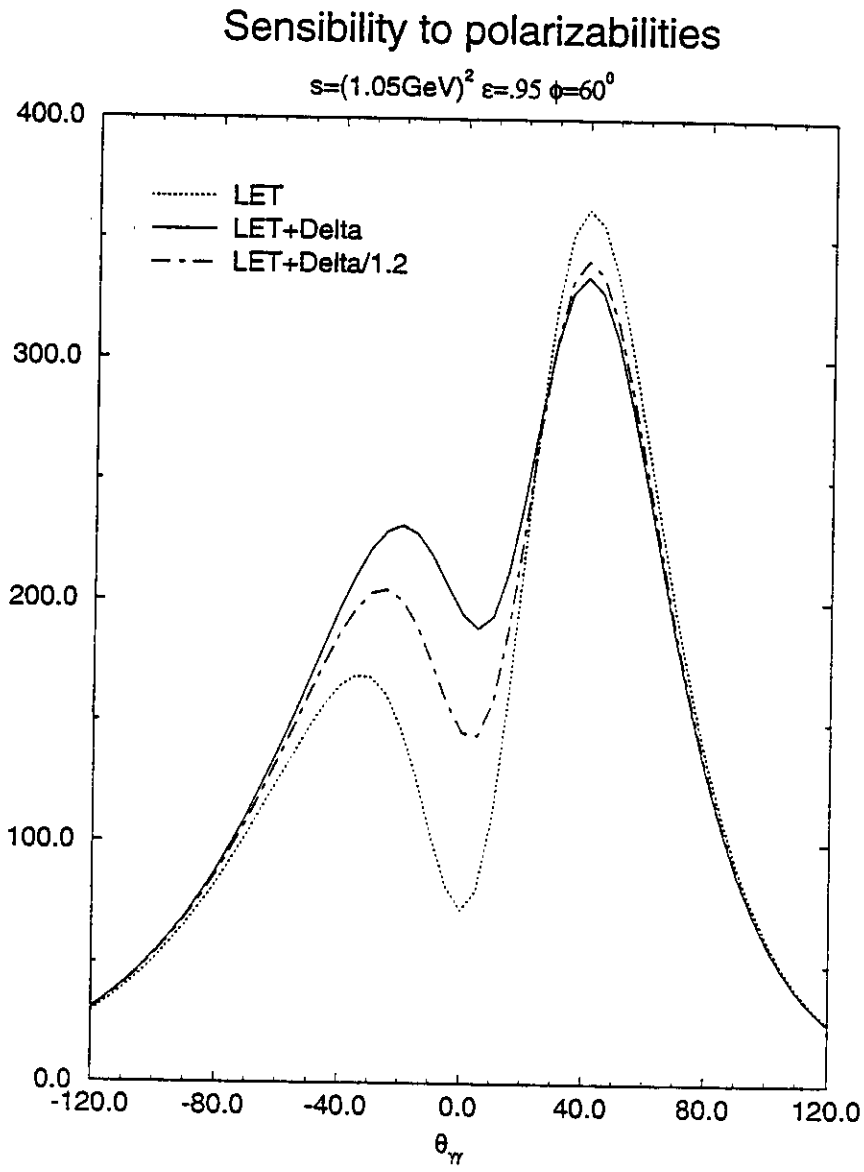

Figure 11: Sensitivity of low energy cross section $d\sigma/(dE'_e d\Omega'_E d\Omega'_e)$ (nb GeV^{-1} sr^{-2}) to $Q^2 = 1$ GeV^2 magnetic polarizability (Eq. 12). The BH and VCS amplitudes are added coherently at $\phi = 60°$.

3 Experimental aspects

3.1 Apparatus

3.1.1 Spectrometers

We will make use of the two spectrometers of the hall A in their standard configuration as describe in the table 4.1 of [22]. Standard electron and proton identification will be used.

3.1.2 Targets

Thanks to the CEBAF high duty cycle, we are not limited by accidental $(e,e') \times (e',p)$ coincidence rates, nor by singles rates (0.5 MHz) and we will use therefore a luminosity of $10^{38}\ cm^{-2}s^{-1}$. This corresponds to $40\mu A$ beam current on a 10 cm long liquid hydrogen target. We will use the high power cryogenic target developed for the hall A. Its specifications can be found in table 8.3 of ref [22]. No modification of the vacuum target chamber is required.

3.2 Simulation of the experiment

In this section, we present and justify our hypotheses for estimating the counting rates in the resonance region.(For the region below the pion threshold we have of course taken the amplitude given by the LET for VCS and the exact expression for BH.)

3.2.1 VCS cross section evaluation in the resonance region

The cross section of VCS, when the BH amplitude is negligible, can be written as [23]:

$$\frac{d^5\sigma}{dk'd\Omega'_e dtd\phi} = \Gamma(k,k',\theta'_e) \times \frac{d^2\sigma(s,Q^2,t)}{dtd\phi} \tag{13}$$

where Γ is the virtual photon flux factor and $d^2\sigma(s,Q^2,t)/dtd\phi$ the cross section of photo-production by a virtual photon. We have:

$$\Gamma(k,k',\theta'_e) = \frac{\alpha}{2\pi^2}.\frac{k'}{k}.\frac{(s-M^2)}{2M}.\frac{1}{Q^2}.\frac{1}{(1-\epsilon)} \tag{14}$$

$$\epsilon = (1+2\frac{\vec{q}^2}{Q^2}\tan^2\theta'/2)^{-1} \tag{15}$$

$$\frac{d^2\sigma(s,Q^2,t)}{dtd\phi} = \frac{d\sigma_T}{dtd\phi} + \epsilon\frac{d\sigma_L}{dtd\phi} + \epsilon\frac{d\sigma_{TT}}{dtd\phi}\cos 2\phi + \sqrt{\epsilon(1+\epsilon)}\frac{d\sigma_{LT}}{dtd\phi}\cos\phi \tag{16}$$

The counting rates that we give for VCS, in absence of any experimental result, are estimated from real Compton scattering data (Figure 2 and [5]), according to the following approximations:

1. Only the transverse part is taken into account:

$$d\sigma_L = 0,\ d\sigma_{TT} = 0,\ d\sigma_{LT} = 0$$

   This strong assumption, which gives conservative counting rates, is supported by 2 facts:

   - In the deep inelastic region, the ratio $R = \sigma_L/\sigma_T$ is small (≤ 0.2).
   - In electroproduction of the pion the longitudinal part of the cross section is important only at low value of t ($|t| < .3GeV^2$) and the interference parts σ_{TT} and σ_{LT} are always small [23].

2. We neglect any dependence in $\cos\theta^{\gamma}_{cm}$ for the VCS cross section. The value of the cross section $d\sigma_T/dt$ is taken at $\theta^{\gamma}_{cm} = 90^0$, angle between the scattered and virtual photon, where experimentally the cross section of real Compton seems to be minimum (Figure 2). Thus our estimate is conservative.

3. The s dependence is taken as s^{-6} according to the scaling law which is approximately satisfied in our energy range by real Compton scattering (Figure 2).

4. No dependance on Q^2 is assumed for the virtual cross section which is taken equal to its value at $Q^2 = 0$. This is supported by the calculation of [34] which indicates that in the backward direction the variation between $Q^2 = 0$ and $Q^2 = 2\ GeV^2$ is only a factor of 2 at $s = 2$ GeV (Figure 9).

In summary, we have taken:

$$2\pi s^6 \frac{d\sigma_T(Q^2,s,t)}{dtd\phi} = 30\mu b \cdot GeV^{10} \tag{17}$$

3.2.2 Check of our evaluation

To verify that our estimate at $Q^2 \neq 0$ is correct, we checked it at $s = 2.356GeV^2$ where the electroproduction of the resonances S_{11} and D_{13} has been measured [12]. We assume that the VCS cross section is dominated by the excitation of the two resonances multiplied by the branching ratio of decay of the resonance in γp.

$$\frac{d\sigma}{d\cos\theta_{cm}d\phi} = \frac{1}{4\pi} \times (\sigma_T^{S_{11}}(Q^2) \times Br(S_{11} \rightarrow p+\gamma) + \sigma_T^{D_{13}}(Q^2) \times Br(D_{13} \rightarrow p+\gamma)) \tag{18}$$

$Q^2(GeV^2)$	.1	.5	1.	2.	3.
$\frac{2\pi s^6 d\sigma}{dtd\phi}$ $(\mu bGeV^{10})$	92.	36.	13.	2.6	.8

Table 1: Prediction for the transvere cross section of VCS at$s$ = 2.36 GeV^2, using the data of [12] on the S_{11} and D_{13} resonance. This is to be compared with the 30 $\mu b\ GeV^{10}$ used in the estimation of Eq. 17.

The parametrization of the result of F.W. Brasse et al. [12] is

$$\sigma_T^{S_{11}}(Q^2) = 21.6\ e^{-.385Q^2}\ \mu b \text{ and } \sigma_T^{D_{13}}(Q^2) = 127.4\ e^{-1.6Q^2}\ \mu b$$

$$Br(S_{11} \rightarrow p + \gamma) = (0.15 \pm .05)\% \text{ and } D_{13} \rightarrow p + \gamma) = (0.55 \pm .5)\%$$

The results of our estimation are given in Table 1 for the sum of the S_{11} and D_{13} contributions. The cross section (Eq. 17) that we use in our count rate estimate is smaller than the estimate of Eq.19 at small Q^2, and larger than the estimate at large Q^2. Eq. 18 ignores the non-resonant background, which will increase the cross section.

3.2.3 π^0 electroproduction cross section

The physical backgrounds we have to consider in the resonance region are the reactions with one electron and one proton which can be accepted by the apparatus. The closest one to VCS in missing mass is the electroproduction of neutral pions:

$$e + p \rightarrow e' + p + \pi^0$$

This reaction is experimentally separated from $p(e, e'p)\gamma$ by the missing mass resolution (Fig. 3). As a by-product of the VCS measurement, we will also obtain the corresponding data on π^0 production which is an interesting reaction in its own right.

We give now a rough estimate of the π^0 counting rate. We distinguish two cases:

1. $|t|$ and $|u|$ large.

   The π^0 transverse cross section is computed under two assumptions:

   - The π^0 cross section and the π^+ cross section are in the ratio 1:2 following the prediction of O.Nachtman [24]. This leads to:

$$\frac{d\sigma_T}{dt}(\gamma^v p \rightarrow \pi^+ n) : \frac{d\sigma_T}{dt}(\gamma^v p \rightarrow \pi^0 p) : \ldots$$

$$: \frac{d\sigma_T}{dt}(\gamma^v n \rightarrow \pi^0 n) : \frac{d\sigma_T}{dt}(\gamma^v n \rightarrow \pi^- p) = 8 : 4 : 1 : 2$$

   - The transverse cross section of $\gamma^v p \rightarrow \pi^+ n$ is given by:

$$2\pi \frac{d\sigma_T}{dt d\phi} = \frac{19.6}{(s - M^2)^2} e^{(1.2t)} \mu b.GeV^{-2}$$

     This empirical parametrization given by [23] works from $Q^2 = 0$ to $Q^2 = 3.3$ GeV^2 and $\sqrt{s}$ around 2 and 3 GeV.

2. $|t|$ large and $|u|$ small.

   From R.L. Anderson at al [6] for backward π^0 production we have a cross section which scales with s^{-3} and with a dependence on u given by $e^{1.5u}$. We normalize the cross section from the data at $E_\gamma = 5GeV$ according to

$$2\pi \frac{d\sigma}{du d\phi} = \frac{28 e^{1.5u}}{s^3} \mu b/GeV^{-8}$$

   We have given no dependence in Q^2.

3.2.4 Single counting rates

-Electron .

The counting rate of single electrons takes into account:

- The elastic cross section on the proton.
- The electroproduction of the Δ (1232) and of two resonances at $\sqrt{s} = 1.5$ and 1.7 GeV.
- The deep inelastic cross section.

-Proton .

The proton counting rate is dominated by photoproduction reactions. We estimate it using the CELEG code[26] with a flux of quasi-real photons given by the equivalent radiation length. In CELEG we have the excitation of all the N^* and Δ resonances.

-Accidental coincidences .

From the single rates in each arm, we compute rates for accidental coincidences with the following assumptions:

- Electrons and protons are fully identified, and all the others are rejected.
- The time coincidences peak between the two arms has a full width of two nanoseconds.
- We require the two particles to originate from the same point in the target (spatial coincidence) within $\pm$ 2σ resolution. The transverse resolution for each spectrometer is 1 mm FWHM (table A.4.1 of [22]), and we assume that the spectrometers see an effective length of 100 mm.

  These timing and spatial requirements ensure a very low level of accidental coincidences.

3.2.5 Backgrounds

- Target windows Due to the excellent vertex resolution described above, the unwanted target window contamination can be easily rejected. This is mandatory to be able to detect the small VCS cross section.

- Deuterium contamination The hydrogen used for the experiment may contain some small percentage of deuterium but this is not a major problem. Indeed, though (e,e'p) events on deuterium with high initial proton momenta may fall in the acceptance of the spectrometers, they have $M_X > M_n$.

3.2.6 Experimental resolution

We have estimated the expected experimental resolution on the missing mass squared M_X^2 in two ways: one using the results of the Monte Carlo simulation which we use to determine the acceptance, and the other by differentiation of the equation $M_X^2 = 0$. In Tables 2,3,4, we give the resolving power $m_\pi^2/\sigma(M_X^2)$ which appears to be always larger than 10, allowing thus a clean separation between VCS and π^0 events.

3.2.7 Phase space acceptance in resonance region

In order to determine the acceptance of the two spectrometers, we have simulated the experiment by a Monte Carlo code, using the specification of [22] on angular and momentum resolutions and acceptances. Radiative corrections to the VCS process have been roughly taken into account by allowing the incident and scattered electrons to radiate a second photon. As is well known this produces a spread in the missing mass spectrum, but this is innocuous. The angular peaking approximation and the equivalent radiator for internal bremsstrahlung have been used [13].

In Figure 5 we show the acceptance in CM energy $\sqrt{s}$ and Q^2 for each set up. The smaller area corresponds to smaller epsilon. In our estimation of the accuracy for σ_T we used only the overlapping regions shown on Figure 5. For each set up we divide this overlapping region in 3 bins of about 50 MeV in $\sqrt{s}$. We made the following hypothesis to scale the results obtained with only $\sigma_T \neq 0$:

$$\sigma_L = 0.1 \ , \ \sigma_{LT} = 0.5 \times \sin\theta_{cm} \ and \ \sigma_{TT} = 0.$$

The accuracy we obtain for respectively σ_T and σ_L are 5 to 15% and 50 to 100%. At $\theta_{cm} = 180^0$, due to the large acceptance (the acceptance covers $\theta_{cm}^{\gamma^*\gamma} \geq 140^0$) we are able to perform an azimuthal analysis (ϕ) to control the effect of σ_{LT} on the extracted σ_T. This is important, because the acceptance is not azimuthally symmetric in ϕ.

Concerning the beam time, 1/3 (resp. 2/3)has been allocated to the larger (resp. smaller) value of epsilon. This will be adjusted during the run according to actual counting rates.

3.2.8 Phase space acceptance below the pion threshold

As pointed out in the introduction in Figure 5, the apparatus accepts the major part of the solid angle of the photon in the laboratory, at low s. In this region the Monte Carlo evaluation takes into account the VCS (evaluated through the LET) and the BH processes coherently. Detailed acceptance results are presented in Figs. 12–17) for just one setup ($s = 1$ GeV^2, $Q^2 = 1\ GeV^2$, $\theta_p = -60°$). In these figures we plot the statistics expected with an integrated luminosity of 20 hours times $10^{38}/cm^2/sec$. We to split the phase space into

40 bins in $\cos\theta^{\gamma^*\gamma}$ × 6 bins in ϕ × 8 bins in the final photon energy)

The figures show separately the contribution of the complete cross section and just the virtual compton cross section. Note that in some cases the BH peaks are not well reproduced. This is an unimportant artifact of the simulation. Processes with emission of two real photons are controlled by the missing mass spectrum. Away from the BH peaks, the figures show excellent statistics over a wide kinematic range for which the VCS and BH contributions are comparable.

3.3 Choice of kinematics for the proposed study

The choice of the kinematics was conditioned by the following points:

- The incident energy of the beam is less than 4 GeV.
- The spectrometers are used in the standard configuration. The minimum scattering angle is 12.5^0.
- For the angular distribution at $s = 2.36GeV^2$ and $Q^2 = 1GeV^2$ we restrict to photon angles for which the BH process is not too large with respect to the VCS process.
- For the transverse-longitudinal separation at $\theta^{cm} = 180^o$ we make the balance between the counting rate at low ϵ and the necessity to have the two ϵ very different. We try to have at least $\epsilon_a - \epsilon_b > 0.3$.
- In the resonance region, we choose to center s at 2.36 GeV^2 on the S_{11} where electroproduction data [12] give us a control on the counting rates.

3.3.1 Resonance region

Due to the limitation described above, we can perform the transverse longitudinal (T/L) separation at $\theta^{\gamma^*\gamma} = 180^o$ in the resonance region ($s = 2.36GeV^2$) at invariant momentum transfers Q^2 between 0.2 and 3.5 GeV^2 (Table 3). In order to get a reasonable determination of the longitudinal contribution, we require more than 1000 counts for each setting.

The angular distribution at $s = 2.36GeV^2$ is presented in Table 5. We perform this measurement at the same θ_{cm} angles at $\phi = 0^o$ and $\phi = 180^o$. For this kinematic we require 10^4 events in order to keep opened the possibility of separation between the T, L, TT and TL cross sections. We point out that at ($\theta_{cm}^{\gamma\gamma} = 135^o$, $\phi = 0^o$) the BH process is of the same order (1/3) of magnitude than the VCS. This will allow us to explore the BH-VCS interference. This will be useful to prepare the next generation of experiments.

3.3.2 Region below pion threshold

We choose to study 4 values of Q^2 = 1, 1.5, 2 and 2.5 GeV^2 In this region we cannot use a luminosity larger than 10^{38} because the counting rate in coincidence must be stay below 10 kHz.

3.4 Beam time request

We summarize the beam time request in table 6. We need 470 hours for this first measurement of Virtual Compton Scattering. Including the contingency, we request 22 days of beam in the hall A, at a maximum energy of 4 GeV and 40 μA beam current.

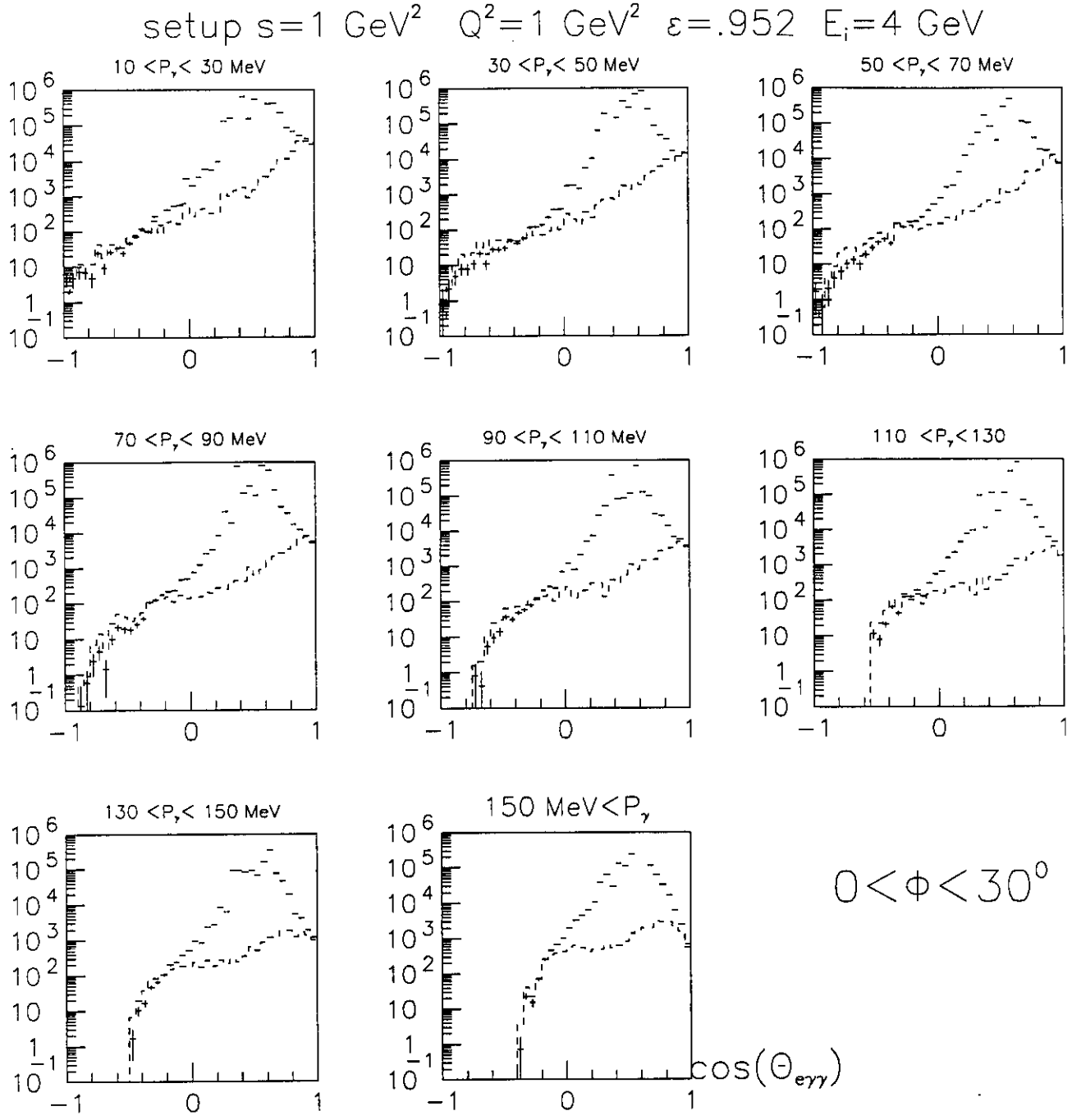

Figure 12: Number of counts for $0\phi < 30°$ per $\Delta \cos\theta^{\gamma^*\gamma} = 0.05$ bin with integrated luminosity of 20 hours $\cdot 10^{38}/cm^2/sec$. Each figure is labeled by the bounds on $p_\gamma = q'$, the final photon energy (lab-frame). The top histogram is the complete rate, the lower histogram is the VCS cross section contribution.

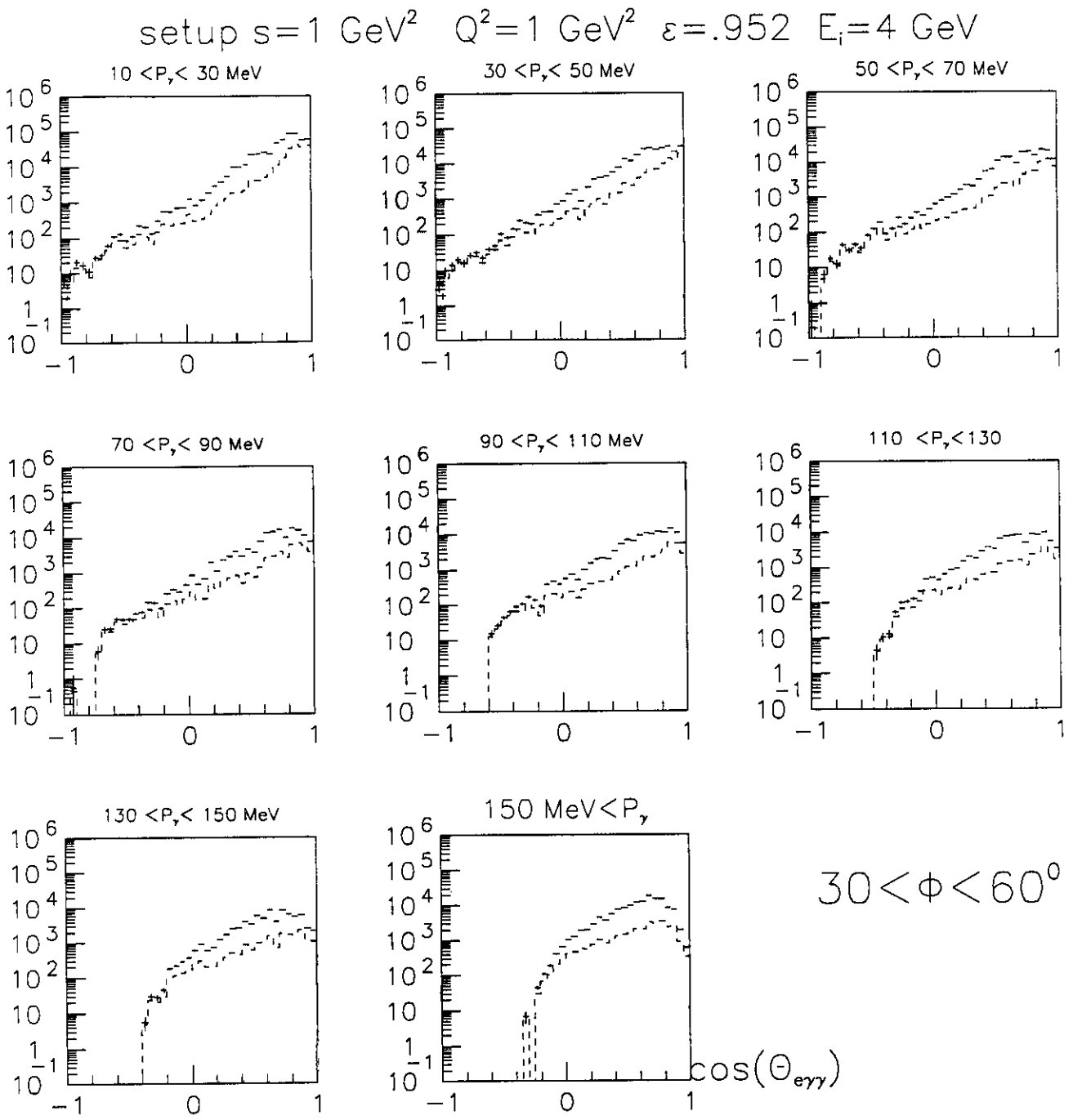

Figure 13: Number of counts for $30° \phi < 60°$ per $\Delta \cos\theta^{\gamma^*\gamma} = 0.05$ bin with integrated luminosity of 20 hours $\cdot 10^{38}/cm^2/sec$. Each figure is labeled by the bounds on $p_\gamma = q'$, the final photon energy (lab-frame). The top histogram is the complete rate, the lower histogram is the VCS cross section contribution.

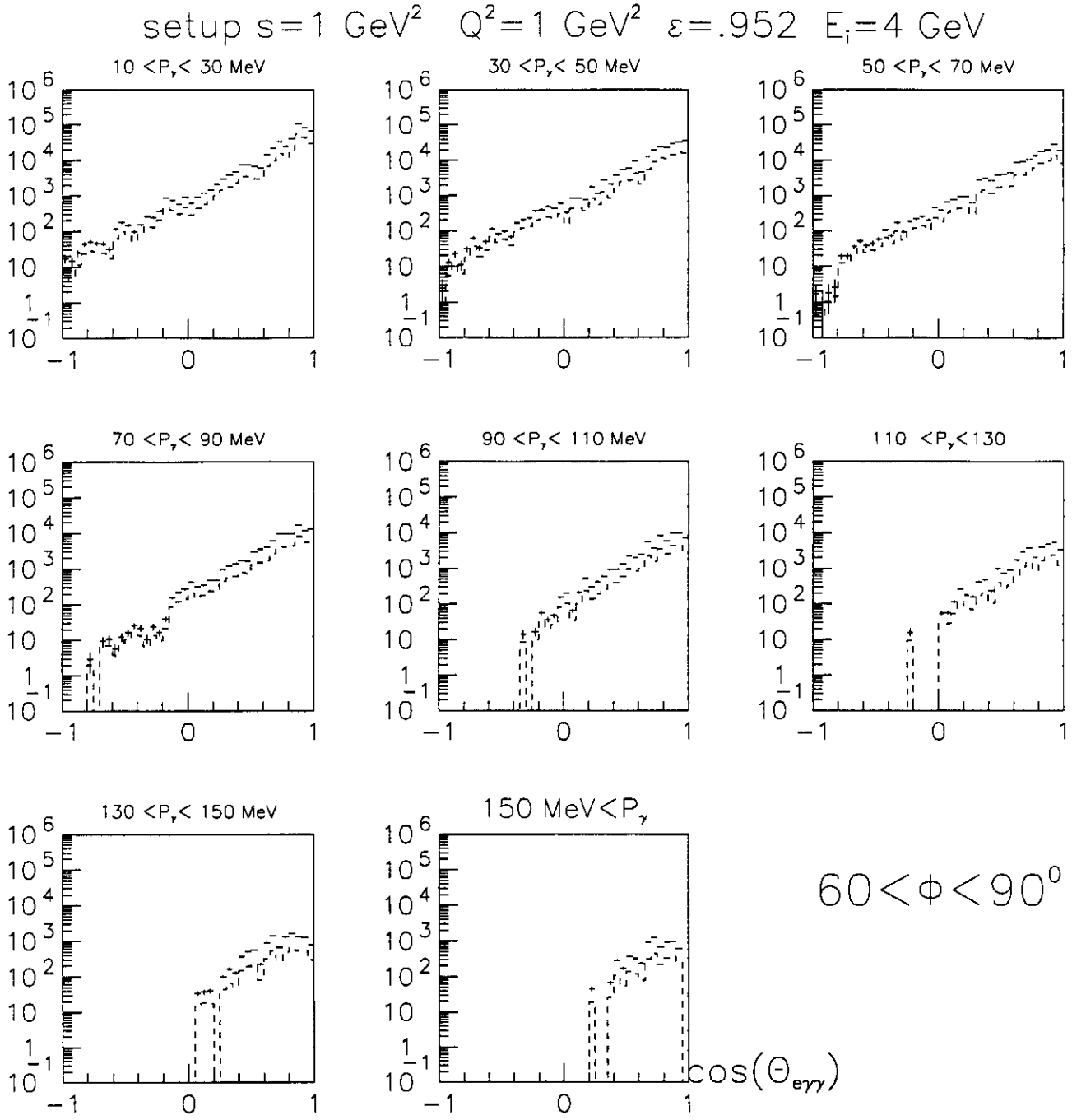

Figure 14: Number of counts for $60°\phi < 90°$ per $\Delta \cos\theta^{\gamma^*\gamma} = 0.05$ bin with integrated luminosity of 20 hours $\cdot 10^{38}/cm^2/sec$. Each figure is labeled by the bounds on $p_\gamma = q'$, the final photon energy (lab-frame). The top histogram is the complete rate, the lower histogram is the VCS cross section contribution.

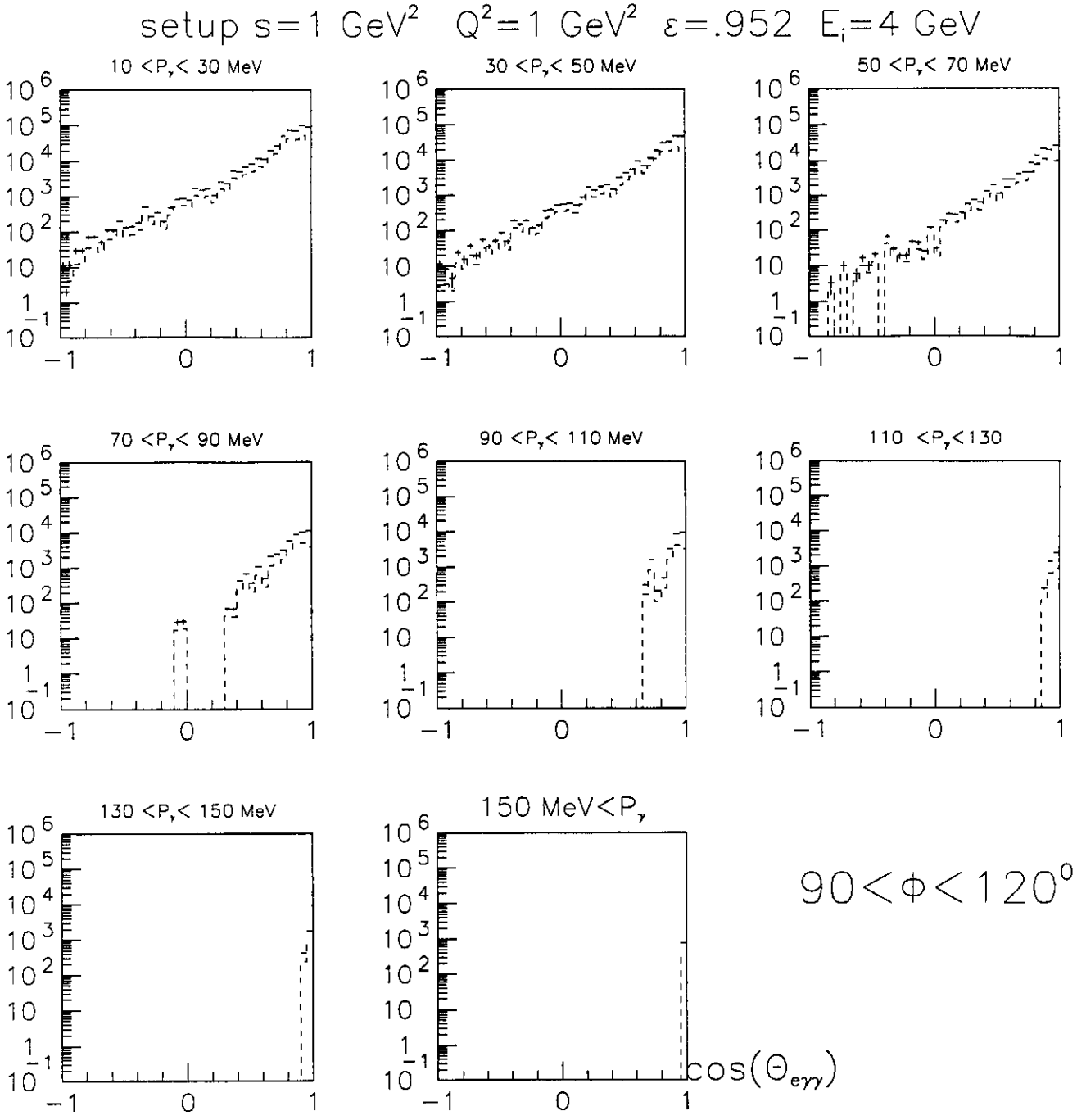

Figure 15: Number of counts for $90° \phi < 120°$ per $\Delta \cos\theta^{\gamma^*\gamma} = 0.05$ bin with integrated luminosity of 20 hours $\cdot 10^{38}/cm^2/sec$. Each figure is labeled by the bounds on $p_\gamma = q'$, the final photon energy (lab-frame). The top histogram is the complete rate, the lower histogram is the VCS cross section contribution.

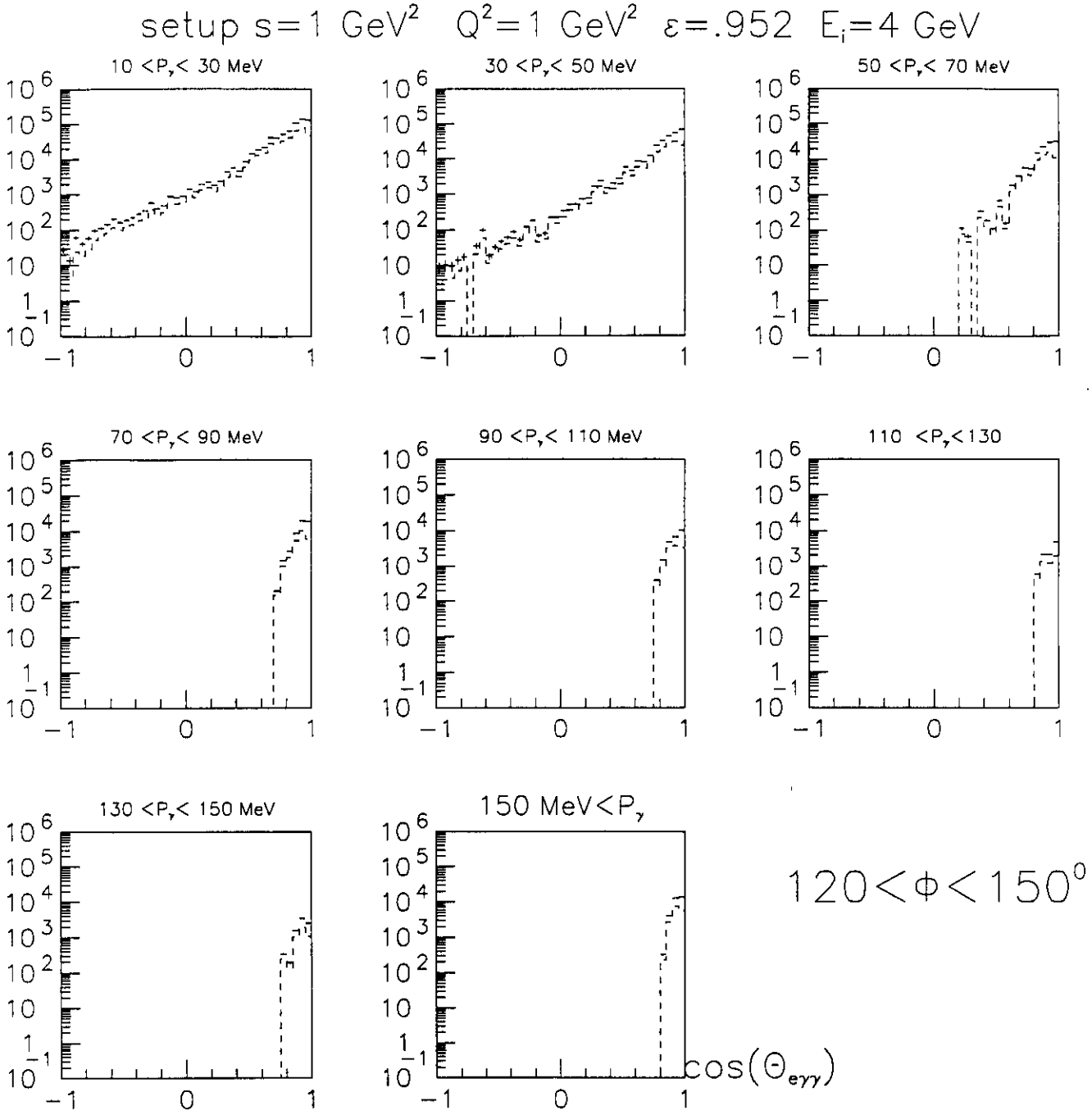

Figure 16: Number of counts for $120° \phi < 150°$ per $\Delta \cos\theta^{\gamma^*\gamma} = 0.05$ bin with integrated luminosity of 20 hours $\cdot 10^{38}/cm^2/sec$. Each figure is labeled by the bounds on $p_\gamma = q'$, the final photon energy (lab-frame). The top histogram is the complete rate, the lower histogram is the VCS cross section contribution.

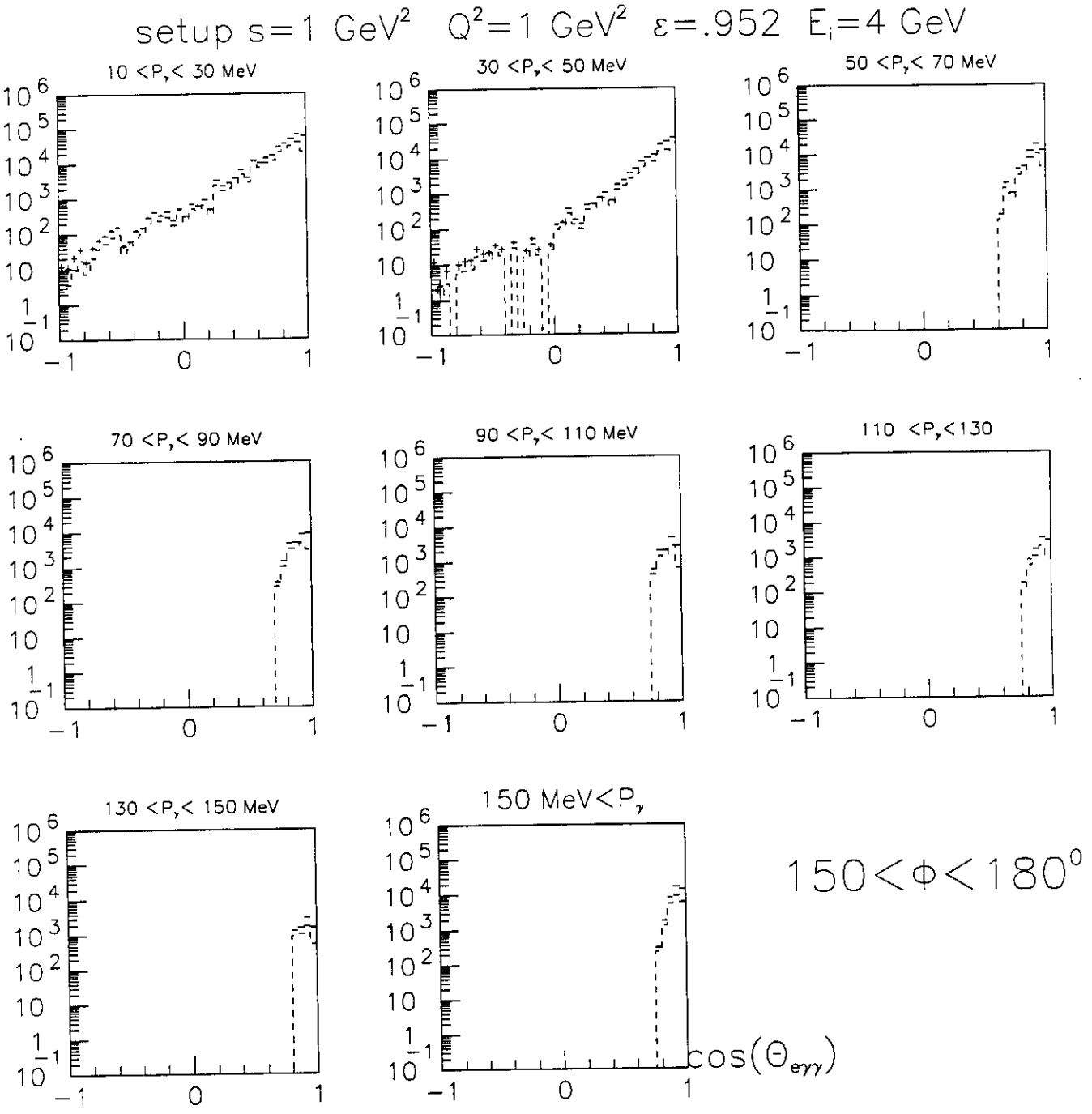

Figure 17: Number of counts for $150°\phi < 180°$ per $\Delta \cos\theta^{\gamma^*\gamma} = 0.05$ bin with integrated luminosity of 20 hours $\cdot 10^{38}/cm^2/sec$. Each figure is labeled by the bounds on $p_\gamma = q'$, the final photon energy (lab-frame). The top histogram is the complete rate, the lower histogram is the VCS cross section contribution.

	s GeV^2	Q2 GeV^2	ϵ	E_i GeV	θ_e degrees	P_e GeV	θ_p degrees	P_p GeV	θ_v degrees	θ^c_γ degrees	P_γ GeV
1a	2.36	0.20	0.89	2.55	12.50	1.65	-20.97	1.26	-20.97	159.0	0.26
1b	2.36	0.20	0.50	1.30	36.16	0.40	-13.67	1.26	-13.67	166.3	0.26
2a	2.36	0.50	0.93	3.82	12.50	2.76	-28.09	1.50	-28.09	151.9	0.23
2b	2.36	0.50	0.45	1.52	49.58	0.47	-16.26	1.50	-16.26	163.7	0.23
3a	2.36	1.00	0.89	4.00	17.57	2.68	-29.21	1.85	-29.21	150.8	0.19
3b	2.36	1.00	0.50	2.04	48.63	0.72	-19.08	1.85	-19.08	160.9	0.19
4a	2.36	2.00	0.76	4.00	27.94	2.15	-25.53	2.48	-25.53	154.5	0.14
4b	2.36	2.00	0.35	2.53	65.74	0.67	-15.23	2.48	-15.23	164.8	0.14
5a	2.36	3.00	0.59	4.00	39.87	1.61	-20.52	3.07	-20.52	159.5	0.12
5b	2.36	3.00	0.30	3.11	70.87	0.72	-13.30	3.07	-13.30	166.7	0.12

	θ_{cm} degres	$N_{Comp.}$ c/h	N_{Beth} c/h	N_e c/s	N_p c/s	Acci. c/h	$\frac{m_\pi^2}{\sigma(M_\tau^2)}$	time h
1a	180	$2.47\ 10^3$	$2.03\ 10^0$	$2.93\ 10^5$	$1.81\ 10^5$	33.2	63.2	20
1b	180	$9.81\ 10^1$	$0.61\ 10^0$	$7.91\ 10^3$	$1.14\ 10^5$	0.4	130.7	
2a	180	$3.52\ 10^3$	$2.08\ 10^0$	$1.83\ 10^5$	$6.43\ 10^4$	8.9	39.8	20
2b	180	$7.08\ 10^1$	$0.44\ 10^0$	$1.79\ 10^3$	$3.85\ 10^4$	0.0	119.5	
3a	180	$2.84\ 10^3$	$1.22\ 10^0$	$2.57\ 10^4$	$1.48\ 10^4$	0.3	44.2	-
3b	180	$1.27\ 10^2$	$0.40\ 10^0$	$8.29\ 10^2$	$3.99\ 10^3$	0.0	103.3	
4a	180	$1.49\ 10^3$	$0.48\ 10^0$	$1.72\ 10^3$	$1.93\ 10^3$	0.0	63.2	30
4b	180	$8.23\ 10^1$	$0.16\ 10^0$	$9.98\ 10^1$	$9.72\ 10^3$	0.0	113.4	
5a	180	$7.07\ 10^2$	$0.32\ 10^0$	$2.18\ 10^2$	$2.39\ 10^3$	0.0	85.2	30
5b	180	$9.96\ 10^1$	$0.10\ 10^0$	$3.30\ 10^1$	$2.39\ 10^3$	0.0	116.0	

Table 2: Counting rates at S=2.36 GeV^2 and $\theta_{cm} = 180^0$.

	s GeV^2	Q2 GeV^2	ϵ	E_i GeV	θ_e degrees	P_e GeV	θ_p degrees	P_p GeV	θ_v degrees	θ_γ degrees	P_γ GeV
1a	2.00	1.00	0.91	4.00	16.97	2.87	-33.74	1.67	-33.74	146.3	0.16
1b	2.00	1.00	0.40	1.66	64.65	0.53	-18.42	1.67	-18.42	161.6	0.16
2a	2.36	1.00	0.89	4.00	17.57	2.68	-29.21	1.85	-29.21	150.8	0.19
2b	2.36	1.00	0.50	2.04	48.63	0.72	-19.08	1.85	-19.08	160.9	0.19
3a	3.00	1.00	0.83	4.00	18.83	2.34	-22.87	2.17	-22.87	157.1	0.23
3b	3.00	1.00	0.40	2.26	50.82	0.60	-13.87	2.17	-13.87	166.1	0.23
4a	3.50	1.00	0.77	4.00	20.01	2.07	-19.03	2.43	-19.03	161.0	0.26
4b	3.50	1.00	0.41	3.50	44.48	0.67	-12.50	2.43	-12.50	167.5	0.26

	θ_{cm} $degrees$	$N_{Comp.}$ c/h	N_{Beth} c/h	N_e c/s	N_p c/s	Acci. c/h	$\frac{m_\pi^2}{\sigma(M_x^2)}$	time h
1a	180	$7.14\ 10^3$	$3.80\ 10^0$	$1.76\ 10^4$	$4.08\ 10^4$	0.5	49.2	20
1b	180	$1.41\ 10^2$	$0.90\ 10^0$	$2.14\ 10^2$	$1.51\ 10^4$	0.0	141.6	
2a	180	$2.84\ 10^3$	$1.22\ 10^0$	$2.57\ 10^4$	$1.48\ 10^4$	0.3	44.2	20
2b	180	$1.27\ 10^2$	$0.40\ 10^0$	$8.29\ 10^2$	$3.99\ 10^3$	0.0	103.3	
3a	180	$7.24\ 10^2$	$0.30\ 10^0$	$1.76\ 10^4$	$2.80\ 10^4$	0.3	42.6	40
3b	180	$2.49\ 10^1$	$0.67\ 10^{-1}$	$5.60\ 10^2$	$8.68\ 10^3$	0.0	81.6	
4a	180	$2.38\ 10^2$	$0.90\ 10^{-1}$	$0.98\ 10^3$	$2.00\ 10^3$	0.0	40.8	50
4b	180	$1.42\ 10^1$	$0.30\ 10^{-1}$	$5.70\ 10^2$	$2.00\ 10^3$	0.0	48.0	

Table 3: Counting rates at Q2=1. GeV^2 and $\theta_{cm} = 180^0$.

	θ_{cm} GeV^2	Q2 GeV^2	ϵ	E_i GeV	θ_e degrees	P_e GeV	θ_p degrees	P_p GeV	θ_v degrees	θ_γ degrees	P_γ GeV
1	-120	1.00	0.89	4.00	17.57	2.67	-44.82	1.55	-29.21	39.2	.448
2	-135	1.00	0.89	4.00	17.57	2.67	-40.95	1.67	-29.21	57.7	.341
3	-150	1.00	0.89	4.00	17.57	2.67	-37.03	1.77	-29.21	82.1	.258
4	-165	1.00	0.89	4.00	17.57	2.67	-33.12	1.83	-29.21	113.6	.206
5	180	1.00	0.89	4.00	17.57	2.67	-29.21	1.85	-29.21	161.0	.189
6	160	1.00	0.89	4.00	17.57	2.67	-25.29	1.83	-29.21	-172.1	.206
7	150	1.00	0.89	4.00	17.57	2.67	-21.38	1.77	-29.21	-140.5	.258
8	135	1.00	0.89	4.00	17.57	2.67	-17.50	1.67	-29.21	-116.0	.341
9	120	1.00	0.89	4.00	17.57	2.67	-13.60	1.55	-29.21	-97.6	.448

	θ_{cm} *degrees*	$N_{Comp.}$ c/h	N_e c/s	N_p c/s	Acci. c/h	$\frac{m_\pi^2}{\sigma(M_\pi^2)}$	time h
1	-120	$3.1\ 10^4$	$2.5\ 10^4$	$.9\ 10^4$	0.4	25.0	10
2	-135	$3.9\ 10^3$	$2.5\ 10^4$	$.4\ 10^4$	0.1	23.0	10
3	-150	$3.4\ 10^3$	$2.5\ 10^4$	$.4\ 10^4$	0.1	23.0	10
4	-165	$2.9\ 10^3$	$2.5\ 10^4$	$1.5\ 10^4$	0.4	28.0	10
5	180	$2.8\ 10^3$	$2.5\ 10^4$	$1.5\ 10^4$	0.2	44.0	–
6	165	$2.1\ 10^3$	$2.5\ 10^4$	$1.5\ 10^4$	0.1	75.0	10
7	150	$1.6\ 10^3$	$2.5\ 10^4$	$8.8\ 10^4$	1.4	36.0	10
8	135	$1.0\ 10^3$	$2.5\ 10^4$	$9.0\ 10^4$	2.4	19.0	10
9	120	$7.6\ 10^2$	$2.5\ 10^4$	$1.9\ 10^5$	8.5	12.0	10

Table 4: Counting rates at $Q2 = 1.\ GeV^2$ and $S = 2.36\ GeV^2$.

Q2	ϵ	E_i	θ_e	P_e	θ_p	P_p
GeV^2		GeV	degrees	GeV	degrees	
1.0	.95	4.00	15.6	3.40	-59.7	1.19
1.5	.92	4.00	19.9	3.14	-45.5	1.51
2.0	.87	4.00	24.1	2.87	-40.3	1.82
2.5	.82	4.00	28.4	2.60	-35.9	2.12

Q^2	N_e	N_p	time
GeV^2	c/s	c/s	h
1.0	$1.6\ 10^4$	$.86\ 10^4$	20
1.5	$2.4\ 10^3$	$.12\ 10^4$	30
2.0	$5.1\ 10^2$	$.25\ 10^4$	40
2.5	$1.3\ 10^2$	$.17\ 10^4$	60

Table 5: Counting rates at $Q2 = 1.\ GeV^2$ below the pion threshold

T/L s=2.36 GeV^2, $\theta_{cm} = 180^0$	20, 20, 30, 00, 40 h	110 h
T/L Q^2=1 GeV^2, $\theta_{cm} = 180^0$	20, 20, 40, 50 h	130 h
angular distribution s=2,36 GeV^2, Q2=1 GeV^2	8 × 10 h	80 h
Below pion threshold s=1 GeV^2,Q^2=1., 1.5, 2., 2.5 GeV^2	20 30 40 60 h	150 h
contingency		50 h
TOTAL		**520 h**

Table 6: Beam time request at Lu=10^{38} (LH2 target 10 cm and 40 μA)

References

[1] M. Jung et al., Z. Phys. **C10** (1981) 197

[2] Y. Wada et al., Nucl. Phys. **B247** (1984) 313

[3] T. Ishii et al, Nucl. Phys. **B254** (1985) 458

[4] J. Deutsch et al., Phys. Rev. **D8** (1973) 3828

[5] M.A. Shupe et al. Phys. Rev. **D19** (1979) 1929

[6] R.L. Anderson et al., Phys. Rev. Lett. **25** (1970)1218

[7] D.O. Caldwell et al., Phys. Rev. Lett. **33** (1974) 868

[8] G. Farrar et H. Zhang, Phys. Rev. **D41** (1990) 3348

[9] S.Brodsky and G. Farrar, Phys. Rev. Lett. **31** (1973) 1953

[10] T. Gousset, work in progress

[11] M. Schurmann, work in progress

[12] F.W. Brasse et al., Z. Phys. **C22** (1984) 33

[13] L.W. Mo and Y.S. Tsai, Rev. Mod. Phys. **41** (1969) 205

[14] N. Isgur and G. Karl, Phys. Rev. **D19** (1979) 2653

[15] T. de Grand and C. Rebbi, Phys. Rev. **D9** (1978)2358

[16] P.A.M. Guichon, Phys. Lett. **B164** (1985) 361

[17] J.D. Breit, Nucl. Phys. **B202** (1982) 147

[18] F. Foster and G. Hughes, Rep. Prog. Phys. **46** (1983) 1445

[19] S. Brodsky, in Perturbative Quantum Chromodynamics, A.H. Mueller editor, World Scientific (1989)

[20] S. Frederiksson, in Di-quarks, M. Anselmino and E. Predazzi editors, World Scientific (1988)

[21] P. Kroll, M. Schurmann and W. Schweiger, Nucl. Phys. Int. J. Mod. Phys. **A6** (1991) 4107

[22] Conceptual Design Report, CEBAF, April 1990

[23] P. Brauel et al., Z. Phys. **C3** (1979) 101

[24] O. Nachtman, Nucl. Phys. **B115** (1976) 61

[25] R.L. Anderson et al., Phys. Rev. **14** (1976) 679

[26] D. Joyce, "CELEG", Users Manual CLAS Notes 89004 (1988)

[27] V.A. Petrun'kin, Sov. Phys. JETP, **13** (1961) 808.

[28] F.E. Low, Phys. Rev. **96** (1954) 1428.

[29] E.L. Hallin, Phys. Rev. **D48** (1993) 1497.

[30] A. Zieger et al. Phys. Lett. **B278** (1992) 34.

[31] R. Koniuk and N. Isgur, Phys. Rev. **D21** (1980) 1868, and R. Koniuk and N. Isgur, Phys Rev Lett **44** (1980) 845.

[32] F.J. Federspiel, et al, Phys. Rev. Lett **67** (1991) 1511.

[33] S. Capstick and B.D. Keister, Phys. Rev. **D46** (1992) 84.

[34] S. Capstick and B.D. Keister, Private communication.

[35] P.A.M. Guichon to be published